THE VISIBLE-TO-SHORT-WAVE-INFRAFRED SPECTRUM OF SKYLIGHT POLARIZATION

by

Laura Marie Dahl

A professional paper submitted in partial fulfillment
of the requirements for the degree

of

Master of Science

in

Electrical and Computer Engineering

MONTANA STATE UNIVERSITY
Bozeman, Montana

July 2015

ACKNOWLEDGMENTS

I would like to thank Dr. Joseph Shaw for his guidance and enthusiasm towards this project and Dr. Nathan Pust for his assistance and contributions. I would also like to thank Dr. Daniel A. LeMaster for letting us use the Corvus SWIR-MWIR Polarimeter along with Larry Pezzaniti at Polaris Sensor Technologies, Inc. for technical support. Finally, I am very grateful to my friends and family for all the support they have shown me throughout the course of this project and my educational career.

This material is based on research sponsored by the Air Force Research Laboratory, under agreement number FA9550-14-1-0140. The U.S. Government is authorized to reproduce and distribute reprints for Governmental purposes notwithstanding any copyright notation thereon. The views and conclusions contained herein are those of the authors and should not be interpreted as necessarily representing the official policies or endorsements, either expressed or implied, of the Air Force Research Laboratory or the U.S. Government.

TABLE OF CONTENTS

LIST OF TABLES

LIST OF FIGURES

LIST OF FIGURES - CONTINUED

LIST OF FIGURES - CONTINUED

Figure Page

LIST OF FIGURES - CONTINUED

Figure Page

LIST OF FIGURES - CONTINUED

Figure Page

LIST OF FIGURES - CONTINUED

Figure Page

ABSTRACT

Skylight becomes partially polarized when sunlight is scattered in the atmosphere. The resulting degree of linear polarization (DoLP) depends on the optical wavelength, atmospheric properties (especially aerosol content), and surface reflectance. The degree of linear polarization for a clear sky was calculated previously for the visible-to-near-infrared (VNIR) spectral range using a successive-orders-of-scattering radiative transfer model and the calculations were validated through comparison with measurements from an all-sky polarization imager. Results from that study showed that VNIR skylight polarization in the visible to the near-infrared spectrum could trend upward, downward, or even have unusual spectral discontinuities that arose because of sharp features in the optical properties of underlying surface and atmospheric aerosols. However, the results were limited to wavelengths below 1 µm from a lack of data at longer wavelengths. This report describes skylight polarization calculations from 0.35 µm to 2.5 µm (visible to SWIR). Inputs to the model included spectral extrapolations of aerosol properties retrieved from a ground-based solar radiometer and measurements of spectral surface reflectance from a hand-held spectrometer. The simulations were run for different environments: a Rayleigh-scattering environment (no aerosol optical depth and no surface reflectance), varied aerosols over a constant-reflectance surface, spectrally constant aerosols over varied surfaces, and a set of more realistic environments that coupled different measured surface reflectance spectra with actual aerosol conditions. Results showed skylight polarization dependence on aerosols and surface reflectance when one element was added, changed, or taken out of an environment. The results were also compared against skylight polarization measurements taken with a SWIR-MWIR polarimeter. Polarization results in the SWIR were highly dependent on the aerosol size distribution and the resulting relationship between the aerosol and Rayleigh optical depths. Once the aerosol optical depth became greater than the Rayleigh optical depth, the predicted polarization deviated significantly from Rayleigh scattering theory. As aerosol optical depths increased, the degree of linear polarization spectrum generally decreased with wavelength at a rate dependent on the aerosol size distribution. Unique polarization features in the modeled results were attributed to the surface reflectance and the skylight DoLP generally decreased as surface reflectance increased.

1. INTRODUCTION

Overview

Environmental remote sensing and military sensing use optical polarization imaging to retrieve aerosol properties for climate studies and to identify man-made objects in space, in the air, or on the ground [1]. By studying naturally occurring polarized light and its propagation, characteristics unseen by the natural eye can be observed as polarization adds additional information that cannot be seen in an image based on intensity (brightness) and/or spectral features (color). Light propagates as an electromagnetic wave and the polarization of a light wave describes the tendency of its electric field to be found with a particular orientation (often described as a relationship between the $\hat{x}$-directed and $\hat{y}$-directed electric field components). For example, polarized light is predictable in the sense that its polarization state can be determined accurately at one point in time or space from knowledge of the polarization state at another point in time or space.

As seen in Figure 1, different imaging systems viewing the same scene can provide different information. The visible image (left) shows a scene in which trucks are effectively hidden in the tree shadows, whereas the polarized image (right) shows the trucks clearly, demonstrating one example of how polarization can be used for enhanced object detection. While the trucks are the main feature of the polarized image, it is also interesting to see the difference between the ground materials; the brown patches, for instance, are more polarized than the trees.

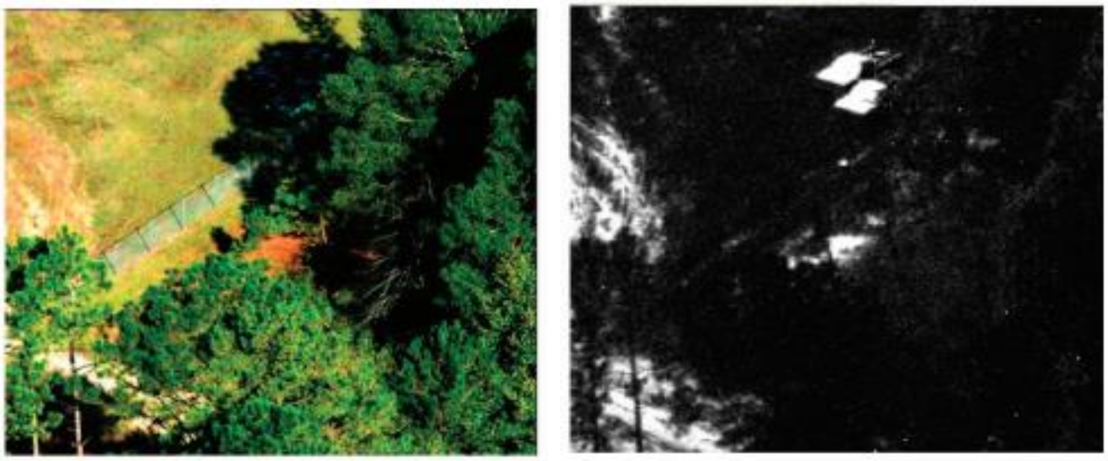

Figure 1. Two imaging methods viewing the same scene. (Left) Visible picture of two pickup trucks hidden in the tree shadows. (Right) Long-wave IR polarization image showing enhanced detection [1]. (Courtesy of Huey Long, U.S. Army Research Laboratory, Adelphi, Maryland.)

Polarization can tell us information about surface features, shapes, shading, and roughness, but only if we properly account for systematic variations related to environmental parameters, such as reflections from smooth water or other naturally smooth surfaces and scattering by clouds [2], atmospheric gases, and atmospheric aerosols. Reflection can be a significant source of polarization at all wavelengths, depending on surface roughness, but atmospheric scattering is a significant source of polarization only at “short” wavelengths relative to the optical wavelength [3]. So, for example, atmospheric radiation is randomly polarized in the long-wave infrared spectral region near 10 µm where thermal emission dominates and it is highly polarized for wavelengths less than 1 µm in the visible and near-infrared region. In this paper, the important question of how atmospheric polarization varies between these two extremes is addressed. Sky polarization in the short-wave infrared (SWIR) spectral region is discussed, along with how it varies with aerosols and surface reflectance (the SWIR spectral band considered here is the wavelength range of 1 to 2.5 µm). Simulations from a successive-orders-of-scattering (SOS) radiative transfer code (validated previously in comparisons with all-sky polarization measurements [4]) were used to model sky polarization in the SWIR.

Atmospheric Polarization

The sun radiates randomly polarized light that becomes partially polarized by scattering within the atmosphere. Tyndall's "incipient cloud" experiment demonstrated that when particles are fine, with size comparable to the wavelength of violet light, maximum polarization occurs at right angles to the illuminating source. He compared his experiment to skylight in the atmosphere and showed that a parallel beam of light once scattered by a particle (incipient cloud) will be observed as blue by an observer perpendicular to the axis of the beam of light [5]. He also concluded that, as more clouds formed in the experimental tube (his controlled atmosphere), the particles in the tube became denser and the polarization of light discharging at right angles became weaker. It was not fully polarized because of multiple scattering within the tube. Multiple scattering destroys perfect polarization that occurs from single scattering events. Tyndall experimentally showed why the sky is blue; however, J.W. Strutt, known as Lord Rayleigh, was the first to quantitatively explain the phenomenon.

Skylight in the clear atmosphere, according to Lord Rayleigh, is actually sunlight scattered by small suspended particles whose size is less than the optical wavelength. If the particles are denser than air, the particle will absorb the incident energy and have transverse vibrations. Lord Rayleigh determined that the irradiance (or intensity) from such scattering is inversely proportional to the fourth power of the wavelength [6] [7]. The scattered radiation is partially linearly polarized, with vibrations perpendicular to the plane of scattering defined by the incident and scattered rays. The degree of polarization (DoP) is represented in Equation 1, where θ is the scattering angle and complete polarization occurs at θ = 90°.

$$DoP = \frac{1-\cos^2\theta}{1+\cos^2\theta} \tag{1}$$

Molecular anisotropy was found to make the maximum DoP in the atmosphere approximately 95% rather than 100% as predicted by Rayleigh scattering theory [8].

Mie scattering theory generally describes the scattering of an electromagnetic plane wave for spherical particles, with Rayleigh scattering being the small-limit approximation for particles much smaller than the optical wavelength [9] [10]. Mie's scattering model assumes the particles are spheres and can be used to find the intensity of scattered light as a series of "partial waves." Mie stated that radiation reflected from a small sphere has a finite number of partial waves, but as the size of the sphere increases, the number of partial waves also increases, making interference occur more often and shifting the maximum polarization forward to a scattering angle of 110^0 for a particle size of 160 μm (compared with Rayleigh particles having maximum polarization at a 90^0 scattering angle). For optically large particles, Mie scattering is roughly independent of wavelength, which is why clouds appear white.

While the classic work of Tyndall, Rayleigh, and Mie demonstrated that skylight polarization depends on the sizes of particles in the atmosphere, Coulson further showed that the degree of polarization of skylight depends on surface reflectance and solar elevation angle in addition to the size and optical properties of scattering molecules and aerosols [11]. As the sun elevation angle changes, the position of the polarization field in the principal plane (plane that passes through the local zenith and through the center of the sun) shifts the location of the maximum polarization approximately 90^0 from the sun. Coulson found that there was a gradual decrease in maximum polarization with increasing sun elevation angle. This effect is a result of increased optical path length between the observer and the location of maximum polarized skylight (this location ‘sets’ toward the horizon as the sun itself rises toward the zenith). Finally, Coulson also showed that surface reflection leads to depolarization of skylight by mixing diffuse surface-reflected light with polarized skylight. Because of this multiple scattering, it is generally found that a higher surface reflectance leads to lower sky polarization.

Kreuter et al. [12] measured the influence of aerosols and surface reflectance on sky polarization using an imaging polarimeter at 450 nm and aerosol products retrieved from the Optical Properties of Aerosols and Clouds (OPAC) database [13]. Surface reflectance measurements were derived from simultaneous global (upward looking) UV radiation spectral measurements in Innsbruck and Svalbard for different environments. At the 450 nm wavelength, the aerosol optical depth ranged from 0.05 to 0.5, with the surface reflectance ranging from 0.1 to 0.75. The study found polarization to be reduced by 30% (70 to 40%) and also found radiance and DoP to be inversely related.

Boesche et al. [14] found that skylight polarization in the O_2A band (755 to 775 nm) was sensitive to aerosol height, surface reflectance, and aerosol optical depth. A higher surface reflectance reduced polarization and this polarization was observed to be generally higher within the O_2A band compared to the surrounding wavelengths. Multiple scattering existed in the atmosphere; however, it was lower inside the band where absorption reduced the scattering path length, therefore making molecular scattering dominant. This study also found that a cirrus cloud had depolarizing effects and that an increase in underlying surface reflectance decreased the DoP in the O_2A band. The surface reflectance effect was observed to be more pronounced for small solar zenith angles since the transmission of the incident sunlight through the atmosphere was stronger and the illumination of the surface greater.

The effect of variable surface reflectance on skylight polarization was further quantified by Dahlberg et al. [15] with all-sky polarization measurements made at the Mauna Loa Observatory on the island of Hawaii. They found a correlation between variations in the maximum degree of polarization over a range of 70 to 85% depending on the underlying surface reflectance. The Mauna Loa Observatory location was chosen for the unique opportunity to observe an extremely clear and clean atmosphere with wide variations in underlying “surface” reflectance as the surrounding dark lava surface was progressively overtaken by clouds that ascended from below nearly each day.

In addition to measurements, models also have been created to determine the DoP and spectral radiance for a clear sky. Lenoble et al. developed an SOS code for solving the vector radiative transfer equation of the earth’s atmosphere with aerosols [16] and this code was validated through comparisons with Montana State University's ground-based, all-sky polarization imager [4]. The model was modified to incorporate aerosol properties determined from solar radiometers in the Aerosol Robotic Network (AERONET) [17]. It was also modified to use MISR satellite land surface Bidirectional Reflectance Distribution Function (BRDF) products to model the surface reflectance. AERONET is a network made up of 700 solar radiometers that measure the direct solar irradiance of skylight at various locations around the world. From these measurements, aerosol optical depths and aerosol properties such as size distributions and complex refractive indices are estimated [18]. A study by Pust et al. [4] found that the simulated degree of linear polarization (DoLP) was slightly but consistently higher than the observed data, which appeared to arise from a 5% underestimation of AERONET-retrieved aerosol refractive index. Differences between the model results and observations were consistent across the entire sky, in regions of high and low DoLP. This difference was removed from a scatterplot of simulated and measured DoLP by increasing the AERONET aerosol real refractive index by 5%; however, this was not tested generally enough to justify a similar correction for all cases.

Pust and Shaw then went on to simulate the wavelength dependence of DoLP in cloud-free skies for the 400-1000 nm spectral range, using model inputs from AERONET and Hyperion satellite retrievals for real environments [19]. The results showed large variations in the wavelength dependence of sky polarization across different earth environments. Accurate modeling of the sky DoLP depended largely on the surface and aerosols in the model, but there was no analysis performed on how the surfaces or aerosols individually caused the variations in the wavelength dependence of sky polarization.

While multiple experiments and modeling efforts have studied the DoLP in the visible spectrum with changing surface reflectance and aerosols, there is extremely limited information regarding the DoLP in the short-wave infrared (SWIR) spectrum. This paper reports the use of the previously validated SOS model to study spectral variation of skylight DoLP from 0.35 to 2.5 µm (i.e., visible to SWIR) using AERONET-retrieved aerosol properties and hand-held spectrometer surface reflectance measurements. In this case, the study focus was on digitally turning individual “knobs” to see how skylight polarization changed as aerosol and surface properties were changed individually (a luxury that cannot be found in nature). This measurement-driven modeling study explored the visible-to-SWIR spectrum of skylight polarization with environments having: no aerosols or surface reflectance; varied aerosols over a spectrally constant-reflective surface; spectrally constant aerosols with varied surface reflectance; and a set of more realistic environments with aerosol parameters from three test days with measured surface reflectance.

This paper proceeds as follows. Chapter 2 presents the study methods, describing the SOS code and the measurements that were used as inputs to simulate controlled but realistic environments. Chapter 3 presents the results of the simulations when exploring independently and jointly changing aerosol and surface properties. Chapter 4 presents a comparison of simulations with SWIR polarimetric images of the sky, and Chapter 5 offers conclusions.

2. METHODS

Model Overview

A modified version of the SOS code developed by Lenoble et al. [16] was used to model the maximum degree of linear polarization in the sky. The model used AERONET data products and MODTRAN atmospheric transmission spectra to represent the atmospheric constituents and represented the surface with reflectance spectra measured with a hand-held spectrometer. A flow chart of the simulation procedure is shown in Figure 2.

A scattering matrix computed from AERONET-retrieved aerosol parameters was used to describe the change of direction, intensity, and polarization of a light beam caused by a single scattering event. This is a function of the scattering angle and depends on the wavelength, the refractive index, the size distribution, and the shape of the scattering particles. Spherical particles were assumed and Mie scattering theory was applied. The solar zenith and azimuth angles were also inputs to the model in order to determine the principal plane of polarization with respect to the sun (plane encompassing the sun, observer, and scattering object).

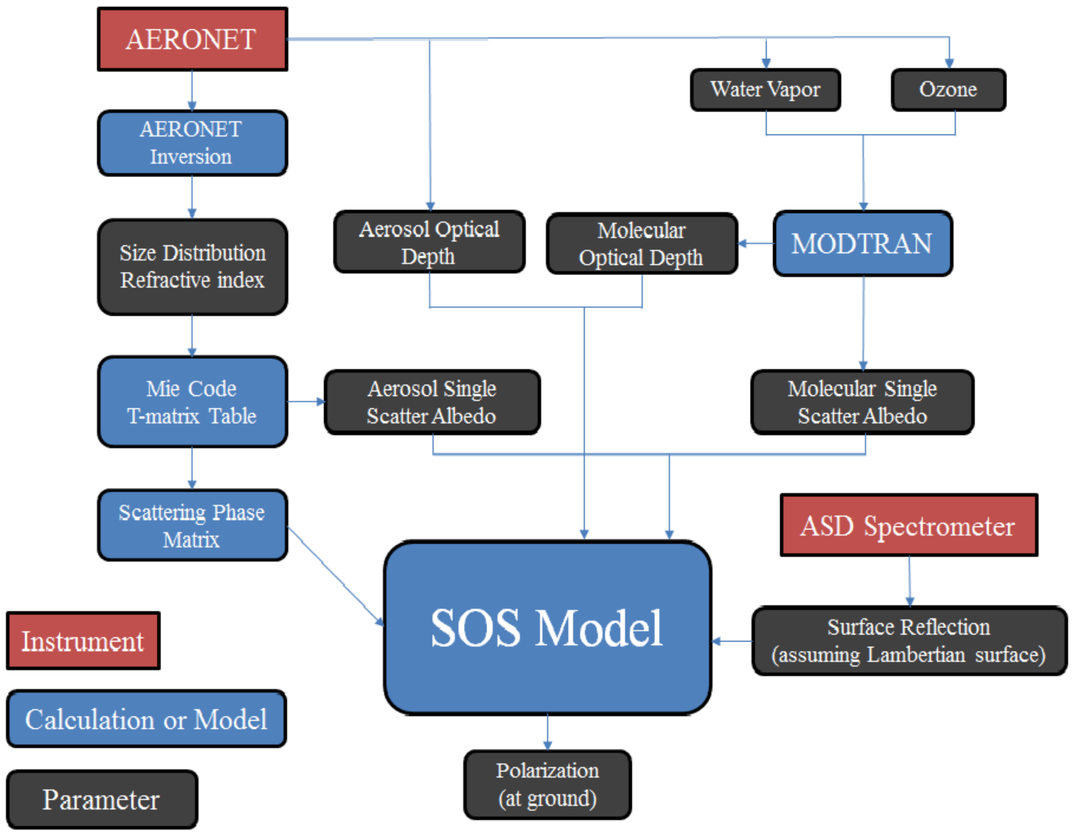

Figure 2. SOS model with input parameters from AERONET data products, MODTRAN transmission spectra, and ASD Spectrometer surface reflectance measurements. The output was a Stokes vector, which was used to determine the DoLP of skylight viewed from the ground.

The model output provided a Stokes vector *S*, containing four Stokes parameters (Equation 2), which were used to determine the skylight DoLP observed from the ground (Equation 3). The Stokes parameters characterize the polarization state of light, with S_0 representing the total radiance [W/(cm^2 sr)] in both the *x* and *y* polarization states. The Stokes parameters S_1 and S_2 describe linear polarization in vertical vs. horizontal and 45° vs. 135° directions, respectively, and S_3 describes the circular polarization of the light beam. Note that S_0, S_1, S_2, and S_3 are also sometimes represented by I, Q, U, and V.

$$S = \begin{pmatrix} S_0 \\ S_1 \\ S_2 \\ S_3 \end{pmatrix} = \begin{pmatrix} I_{0^\circ} + I_{90^\circ} \\ I_{0^\circ} - I_{90^\circ} \\ I_{45^\circ} - I_{135^\circ} \\ I_+ - I_- \end{pmatrix} \quad (2)$$

$$DoLP = \frac{\sqrt{{S_1}^2 + {S_2}^2}}{S_0} \quad (3)$$

In this study, we were interested in observing the maximum DoLP in the SWIR spectral region, along with its dependence separately on surface reflectance and aerosol properties. The zenith and azimuth angle of the sun in our simulations were kept constant at 49° and 118°, respectively, by simulating data from our chosen reference measurement time of 18 August 2014 at 10:34:22 AM (MDT). Aerosol products were retrieved by using AERONET algorithms and measurements taken with a Cimel solar radiometer located in Bozeman, Montana (45.7 °N, 111.0 °W; elevation 1507 m). Figure 3 shows the instrument in its operating location at Montana State University in Bozeman with the Bridger Mountains in the background [20]. The model sun position was confirmed with the National Oceanic and Atmospheric Administration (NOAA) Solar position calculator [21].

Figure 3. CIMEL solar radiometer located in Bozeman, Montana used by AERONET to retrieve atmospheric data products. The left-hand photo also shows the all-sky polarization imager (photos by Joseph A. Shaw).

Surface Reflectance

The surface reflectance measurements used in the model were taken with an ASD field-portable FieldSpec® Pro Spectroradiometer. It uses a fiber optic input with a conical field of view of 25°. The ASD spectrometer adjusted its integration time automatically to give the maximum allowable signal without saturation. Surface reflection was measured as the actual fraction of incident light that was reflected from the measured surface material, relative to a Spectralon reference panel under the same illumination [22]. Measurements were taken with the fiber optic approximately 1 m from the ground and pointed perpendicular to the ground.

In this study we modeled the surface as a uniformly reflective Lambertian surface. Ideally, realistic cases would take viewing geometries and BRDFs into account and an image would contain multiple surface materials. However, we were concerned with the general dependence of polarization on different surface reflectances and wanted to see what trends occurred, so the simple surface reflectance model was sufficient. A golden-yellow wheat field (Figure 4), green grass, sand, and a wood surface (Figure 5) were measured on 18 August 2014 in Bozeman, Montana.

Figure 4. Golden-yellow wheat field photographed on 18 August 2014 in Bozeman.

Figure 5. Green grass and wood surface photographed on 18 August 2014 in Bozeman.

The different surface reflectance measurements for these materials can be seen in Figure 6. Surface parameters were interpolated across strong atmospheric absorption features where accurate measurements could not be obtained. The wood and sand surface reflectance measurements are interesting since they increase with wavelength. For green vegetation, the absorption bands of chlorophyll are responsible for low reflectance values in the blue-yellow (λ = 0.4 to 0.55 μm) and red (λ = 0.65 to 0.69 μm) regions [11] [23]. In between these wavelengths, we see a small increase in reflectance which results from the vegetation absorbing less green light. Backscattering due to the spongy mesophyll leads to an increase in reflectance at approximately λ = 0.70 μm due to plant pigments absorbing less of the radiation entering the leaf. Absorption by liquid water in the leaves causes the low reflectance at wavelengths beyond λ = 1.3 μm. As seen in the wheat field reflectance spectrum, in seasonal senescence (fall) the chlorophyll production decreases, which leads to a lack of pigmentation and reduced absorption in the chlorophyll bands, leading to higher reflectance in the green and red spectra. The yellow color of the wheat field is a result of this phenomenon.

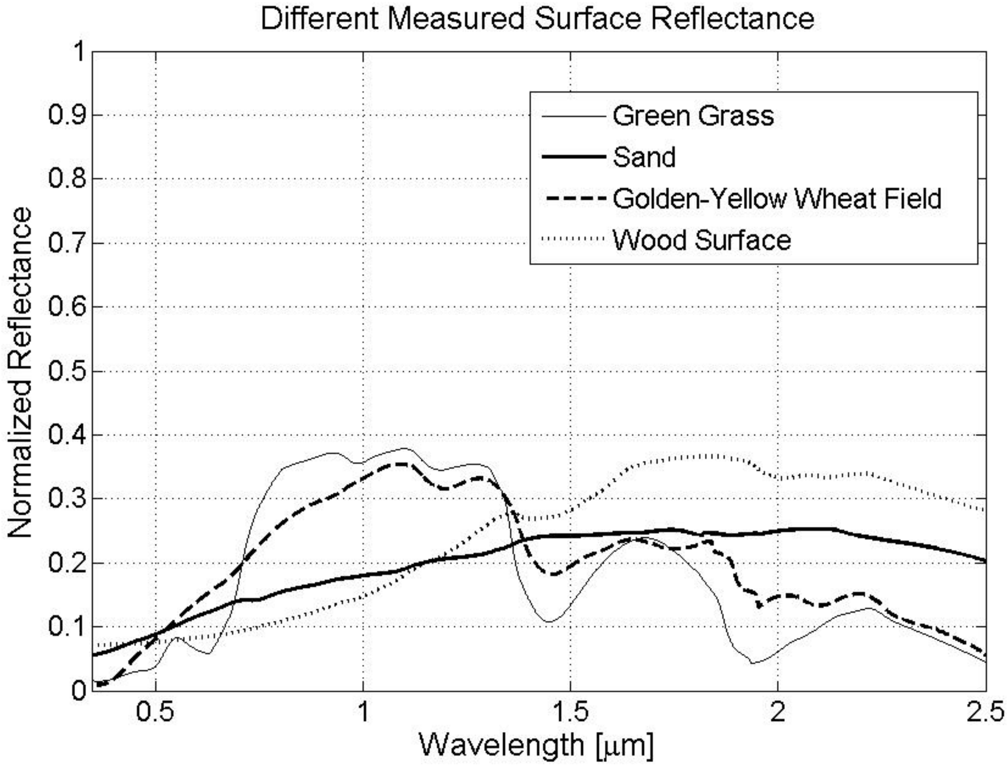

Figure 6. ASD spectrometer reflectance spectra for green grass, sand, a golden-yellow wheat field, and wood surface. The wheat field and green grass spectra are similar, as they are both plant-based materials that absorb in the same wavelength regions.

AERONET Data

Aerosol products were retrieved from the Cimel solar radiometer located in Bozeman. The aerosol phase matrices for scattering can affect the degree of polarization and the matrices are dependent on particle size and complex index of refraction [11]. These parameters, along with the Rayleigh, aerosol, ozone, NO_2, and total optical depths were retrieved from AERONET data. A phase scattering matrix was created using the AERONET particle size distribution, assuming spherical particles to determine the aerosol single scatter albedo, which describes the ratio of aerosol scattering to total extinction (scattering plus extinction). AERONET parameters were available for the following wavelengths: 340 nm, 380 nm, 440 nm, 500 nm, 675 nm, 870 nm, 1020 nm, and 1640 nm.

The Bozeman AERONET instrument only measures optical depths up to 1640 nm, so extrapolation using Angstrom's turbidity formula was performed to extend the simulation measurements to 2500 nm. The Angstrom exponent describes the slope of a log-log plot of optical depth (τ) measured at two wavelengths (λ), according to Equation 4 [24]. The optical depth is a quantitative parameter that represents the degree to which aerosols, Rayleigh particles, and absorption by gases prevent the transmission of light by absorption or scattering and is derived from the Beer-Bouguer-Lambert's law.

$$\alpha = \frac{-\ln\left(\frac{\tau_1}{\tau_2}\right)}{\ln\left(\frac{\lambda_1}{\lambda_2}\right)} \tag{4}$$

Optical depth measurements at the wavelengths of 1020 nm and 1640 nm were used to estimate the Angstrom exponent, which was then used in Angstrom's turbidity formula (Equation 5) to estimate the optical depth at 2500 nm from the reference optical depth at 1640 nm.

$$\tau_\lambda = \tau_0 \left(\frac{\lambda}{\lambda_0}\right)^{-\alpha} \tag{5}$$

Interpolation between the data points was then performed to obtain optical depth values with 1 nm spectral resolution. Extrapolation and interpolation were performed to find the range of Rayleigh, aerosol, and total optical depths from 350 to 2500 nm. The results of the aerosol optical depth extrapolation and interpolation can be seen in Figure 7 for the following cases: low aerosols (19 October 2014), medium aerosols (18 August 2014), and high aerosols (3 August 2014) with reference images in Figures 8, 9, and 10, respectively, showing the cases visually. A low aerosol optical depth represents a clean atmosphere, a medium aerosol optical depth represents a slightly hazy atmosphere, and high aerosol optical depth represents a smoky atmosphere similar to summer days in Bozeman when wildfires generate large amounts of smoke.

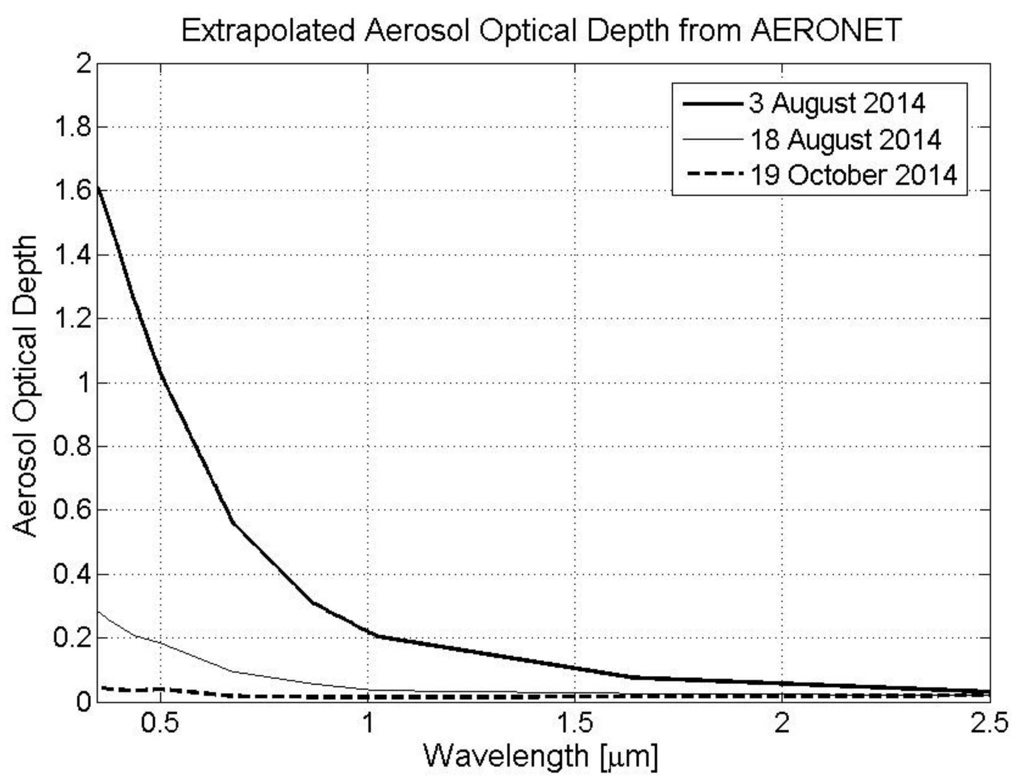

Figure 7. Interpolated and extrapolated AERONET aerosol optical depth for 3 August 2014 (smoky day), 18 August 2014 (moderately hazy day), and 19 October 2014 (clean day) in Bozeman.

Figure 8. “Clean” aerosol case on 20 October 2014. This photograph was taken by Joseph A. Shaw from a plane overlooking Bozeman and it represents a clean aerosol case for 19 October 2014 (both days had similar AERONET data products).

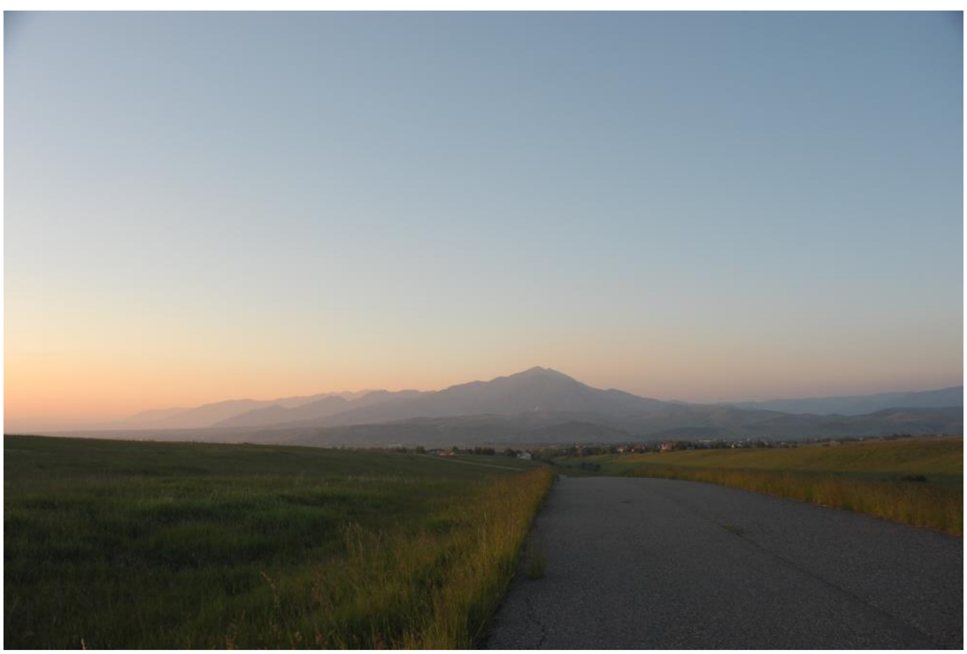

Figure 9. “Hazy” aerosol case on 18 August 2014 in Bozeman (Photographed by Joseph A. Shaw).

Figure 10. “Smoky” aerosol case on 10 August 2014. This photograph was taken by Joseph A. Shaw from a plane overlooking Bozeman. This is a representation of the smoky aerosols on 3 August 2014; however, for 3 August 2014, the aerosol content was higher (AOD of 0.7 to 1.3 compared with 0.07 to 0.7) and the image would have contained more haze.

Figure 11 displays the aerosol volume size distribution retrieved from AERONET inversion algorithms for the following sampled aerosol cases: smoky (3 August 2014), moderately hazy (18 August 2014), and clean (19 October 2014). AERONET measures the number of particles over the entire air column (from the ground at 0 to the top of the atmosphere, effectively infinity). Equation 6 represents the columnar volume size distribution provided by AERONET [25]. The size distribution is used to create the scattering parameters used as inputs to the radiative transfer code.

$$\frac{dV_c}{d\ln r} = \int_{h=0}^{h=\infty} \frac{dV}{d\ln r\ dh} dh \quad [\frac{\mu\text{m}^3}{\mu\text{m} * \mu\text{m}}] \tag{6}$$

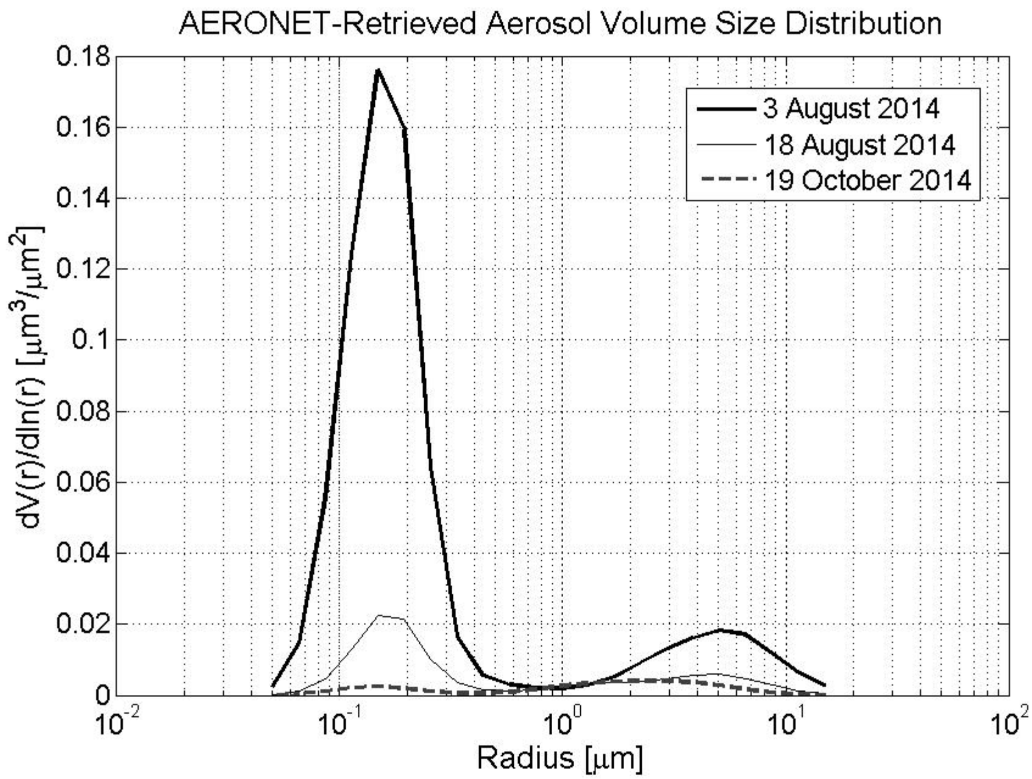

Figure 11. AERONET-retrieved aerosol volume size distribution for 3 August 2014 (smoky day), 18 August 2014 (moderately hazy day), and 19 October 2014 (clean day). The volume size distributions change considerably between the clean and smoky days.

The atmospheric aerosol volume distribution is characterized by a number of modes: the accumulation mode (particle radius ~ 0.05 to 1 µm) and the coarse mode (particle radius ~ 1 to 25 µm) [26]. The particles residing in the accumulation mode are from primary emissions created from forest fires, automobiles, and power plants. The particles in the coarse mode are produced by mechanical processes such as wind or erosion, which stir up dust and pollens. The PM_x (particulate matter with diameters smaller than *x* µm) scale is an air quality control terminology used to indicate the size of the particles in the air. Fine particles with diameters below 10 µm, especially 2.5 µm, can be dangerous and can enter the nose and throat, causing heart and lung issues. For a clean atmosphere, both the accumulation and coarse modes are low and nearly equal size as shown in the volume size distribution for 19 October 2014.

A Mie code and a T-matrix kernel were used to generate a full scattering matrix and the single-scatter albedo parameter from the interpolated size distributions and complex refractive indices shown in Figures 11 and 12, respectively. AERONET provides complex refractive indices for the following wavelengths: 0.440 µm, 0.675 µm, 0.871 µm and 1.018 µm. Extrapolation out to 2.5 µm was performed using a linear fit. Shettle and Fenn report aerosol real refractive index to slightly increase with wavelength for “smoky” days, while the refractive index for “clean” to “hazy” days slightly decreases [27], matching our fit . Beyond 2.5 µm, the aerosol refractive index begins to fluctuate significantly from the aerosol’s rotational and vibrational absorption bands, which if not modeled correctly would lead to variations in the refractive index and errors in the modeled DoLP.

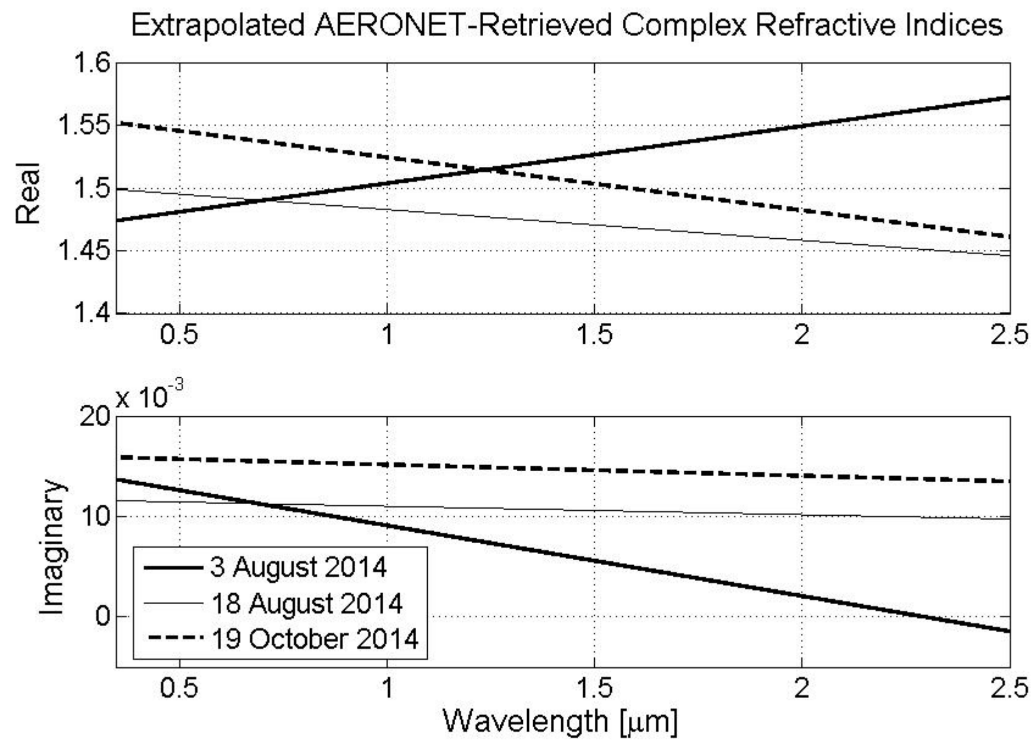

Figure 12. Extrapolated and interpolated AERONET refractive indices for 3 August 2014 (smoky day), 18 August 2014 (moderately hazy day), and 19 October 2014 (clean day). AERONET provided data up to 1.018 µm.

MODTRAN Data

MODTRAN 4.1 transmission simulations were used to calculate the molecular absorption and the molecular single scatter albedo [28]. The precipitable water vapor and ozone values were obtained from AERONET. Atmospheric transmission is related to molecular absorption by Equation 7, where τ_{aer} is the aerosol optical depth, τ_{ray} is the Rayleigh optical depth, and τ_{mol} is the molecular absorption optical depth.

$$T = e^{-(\tau_{aer}+\tau_{ray}+\tau_{mol})} \tag{7}$$

The model was run for a mid-latitude summer atmosphere with no aerosols or clouds. The molecular vertical extinction distribution was set to be exponential with an 8-km scale height in the SOS model. Using the MODTRAN transmission output shown in Figure 13, the molecular optical depth was found using Equation 8 and can be seen in Figure 14.

$$\tau_{mol} = -\log(T) \tag{8}$$

When using MODTRAN molecular absorption parameters in the model, the DoLP is confined to the value of one when the molecular optical depth is infinity, which is a result from the transmission being zero between 1.35-1.42 µm and 1.81-1.95 µm.

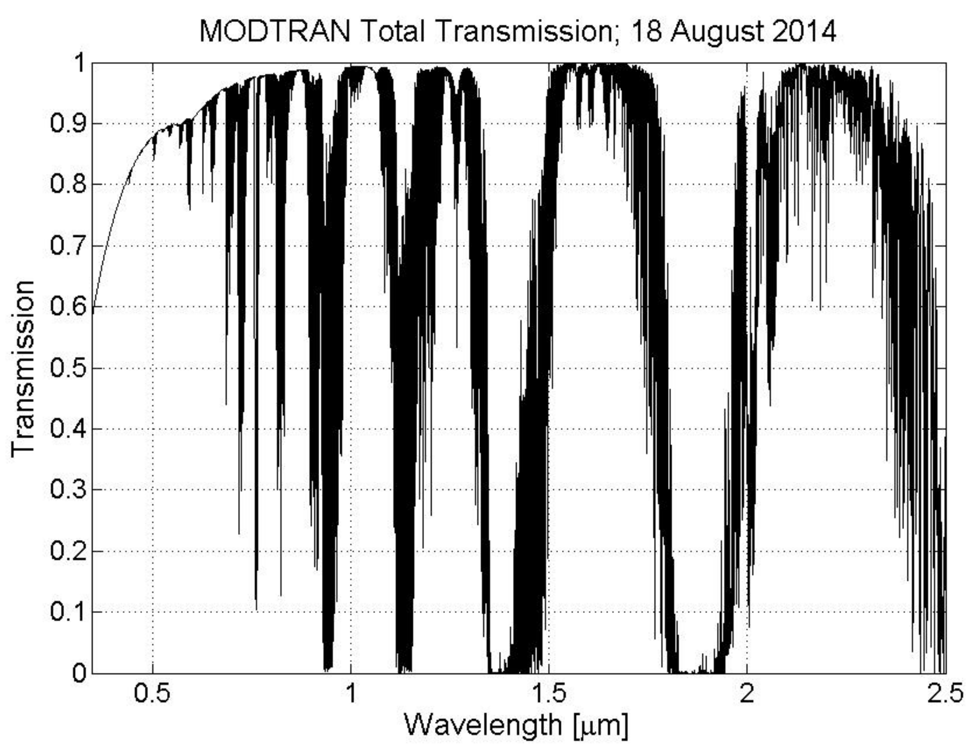

Figure 13. MODTRAN zenith-path atmospheric transmission spectrum used in the skylight polarization simulations.

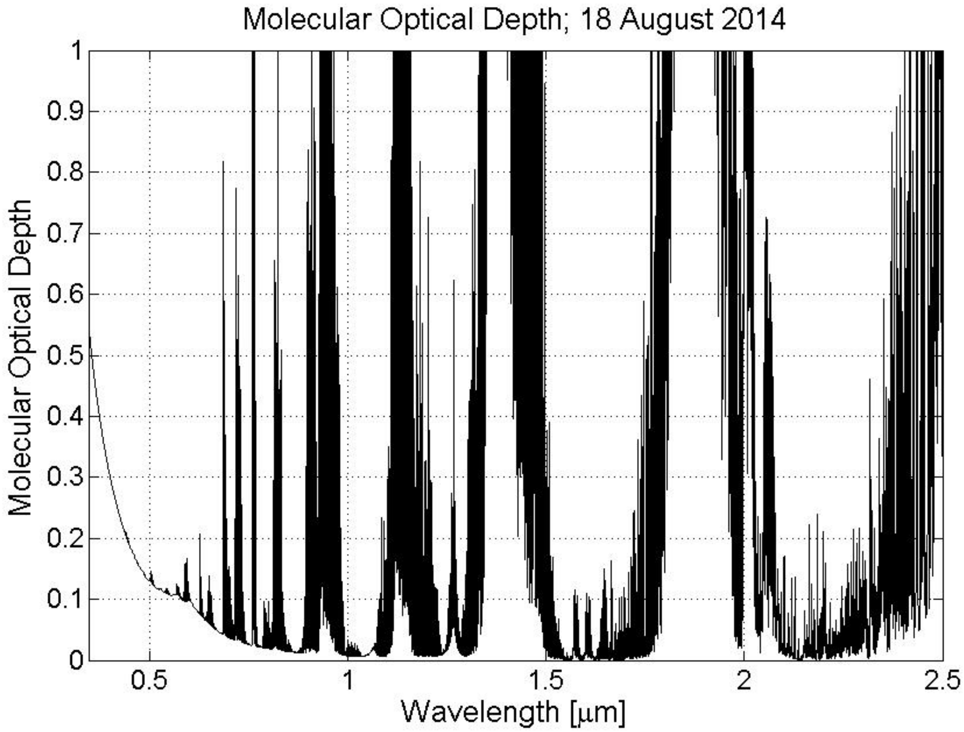

Figure 14. MODTRAN zenith-path atmospheric molecular optical depth spectrum.

The molecular single scattering albedo (molssa) was calculated using Equation 9. If the SOS radiative transfer model was run with no molecular absorption, the molssa and molecular optical depth parameters were found using AERONET data products. The molecular optical depth was found using Equation 10. Figure 15 displays the spectral transmission from molecular scattering. As shown, at wavelengths before 1 μm, molecular scattering is prominent.

$$molssa = \frac{\tau_{ray}}{\tau_{mol}} \tag{9}$$

$$\tau_{mol} = \tau_{total} - \tau_{aer} \tag{10}$$

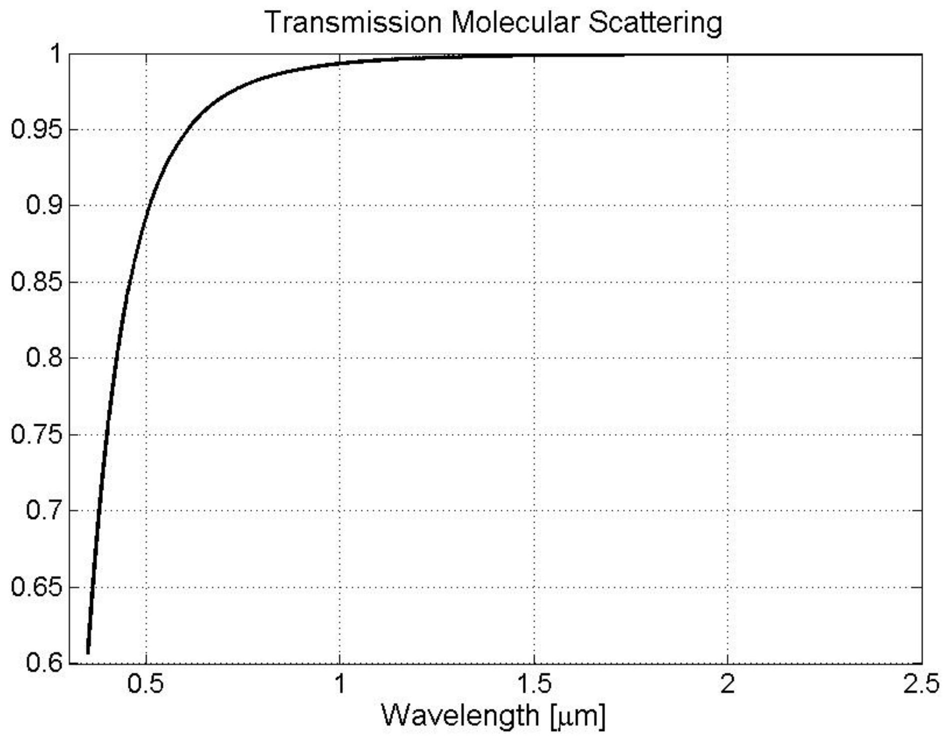

Figure 15. MODTRAN zenith-path atmospheric molecular scattering transmission spectrum.

Atmospheric absorption features are significant in the visible to SWIR polarization spectra and Figure 16 shows the atmospheric absorption lines for 18 August 2014 in Bozeman. The atmospheric transmission absorption bands in this spectral range are mainly from water vapor (H_2O). Table 1 provides a list of the absorption bands present and the percentage to which the transmission falls for the atmospheric absorption lines in Figure 16.

Element	Bands (μm)	Approximate Transmission Percent
Carbon Dioxide (CO_2)	1.4, 1.5, and 2	25
Methane (CH_4)	1.4, 1.5, and 2.3-2.4	95, 85, and 60
Uniformly Mixed Gas	0.6, 0.7, 0.75, 0.25, 1.5, 1.9-2.1, and 2.2-2.5	90, 50, 10, 60, 90, 10, and 60
Ozone (O_3)	0.5- 0.75 and 2.1	0 and 80
Carbon Monoxide (CO) Trace Gases Nitrous Oxide (N_2O)		>98

Table 1: Atmospheric absorption bands from the transmission spectrum in Figure 16. 'Approximate transmission percent' refers to how low the transmission falls in the absorption band. For example, 25% refers to the band starting at 1 and going to 0.25 in the Atmospheric Transmission Absorption Bands spectrum in Figure 16. A trace gas is a gas which makes up less than 1% by volume of the Earth's atmosphere, and it includes all gases except nitrogen (78.1%) and oxygen (20.9%). The most abundant trace gas at 0.934% is argon. Water vapor also occurs in the atmosphere with highly variable abundance.

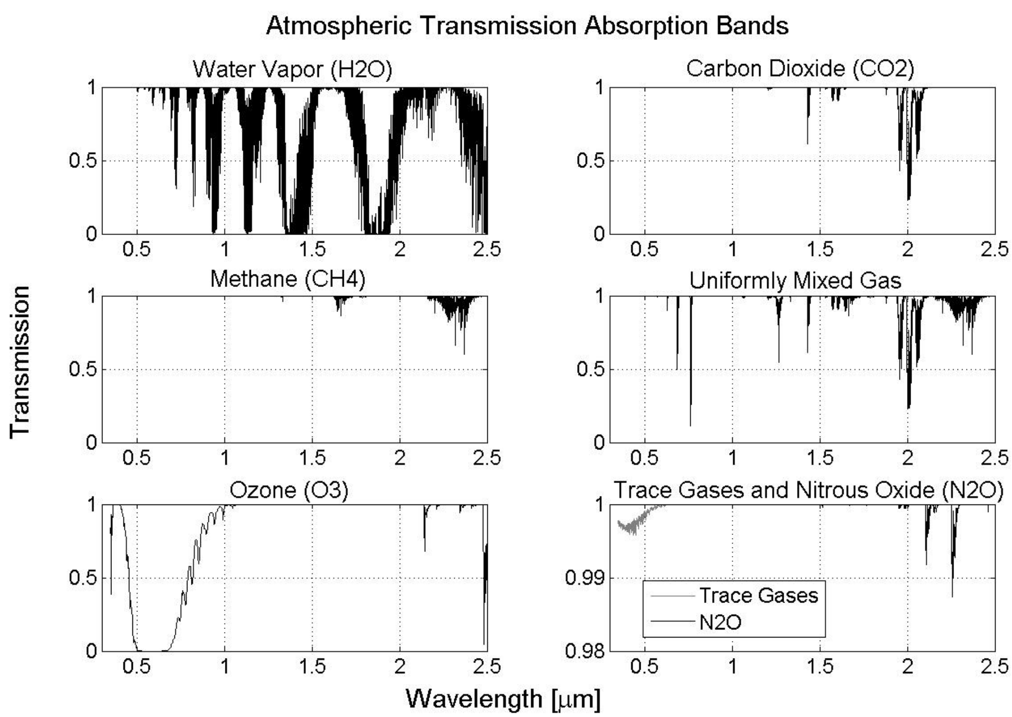

Figure 16. Atmospheric transmission absorption bands for the zenith-path model atmosphere on 18 August 2014 in Bozeman, Montana.

SWIR Polarimeter Measurements

Experimental images were taken with the Corvus SWIR-MWIR imaging polarimeter [30] using filter position 2, representing the wavelength range from 1.5 to 1.8 μm. In the polarimetric mode, the polarizer rotates continuously and measures the Stokes parameters S_0, S_1 and S_2 and the DoLP, and produces a colorfuse image. The S_1 and S_2 images are normalized with respect to S_0. (Note: The polarizer needs to be manually placed on the front of the sensor depending on if SWIR or MWIR images are wanted).

The Corvus SWIR-MWIR imaging polarimeter is a passive sensor that captures images sequentially in time up to 120 frames per second every 45 degrees of rotation. Therefore one frame is captured every 45 degrees. The frame rate was set to 60 frames per second, so the polarizer rotation rate was 2700 degrees per second or 7.5 revolutions per second. The integration time was set accordingly so that there was an average of at least 8000 counts in the raw image (the full dynamic range is 16483 counts) during calibration. Parameter specifications for the imager can be found in Table 2.

Specification	Value
Waveband	1.5-5.0 µm
Camera	FLIR SC6000
FPA format	640 x 512
FPA material	InSb
Pixel Size	25 x 25µm
Objective Lens EFL	100 mm
Lens f/#	2.3
FOV	9.1° x 7.3°
IFOV @ 2 km	0.5 m
Sub-wavebands	1.5-5.0 µm, Filter Position 1
	1.5-1.8 µm, Filter Position 2
	2.0-2.5 µm, Filter Position 3
	3.0-5.0 µm, Filter Position 4

Table 2. Specifications for the Corvus SWIR-MWIR imaging polarimeter.

Gravè, a Polaris Software, recorded the imaging frames through the field of view (FOV) of the sensor. In Gravè, the frame rate, integration time and recordable time could be set, the non-uniformity correction (NUC) could be selected, and S_0, S_1, S_2, DoLP, or colorfuse images could be chosen. The non-uniformity correction was created using the same integration time at which the frames were recorded.

3. MODELED VIS-SWIR SKYLIGHT POLARIZATION MEASUREMENTS

In the visible and short-wave infrared, it has been found that skylight degree of linear polarization can trend upward, downward, and have spectral discontinuities that arise from underlying surface reflectance and atmospheric parameters [19]. The trend of the polarization curve depends on the relative magnitudes of the aerosol and Rayleigh optical depths in the atmosphere, along with the aerosol volume size distribution.

Rayleigh Scattering Case

Rayleigh (molecular) scattering is the main source of skylight for wavelengths below 0.7 µm. The brightness of Rayleigh scattered skylight is inversely proportional to the fourth power of the wavelength. In clean air, skylight spectral polarization is expected to increase with wavelength because at longer wavelengths the amount of multiple molecular scattering is reduced. This conceptual relationship is shown in Figure 17.

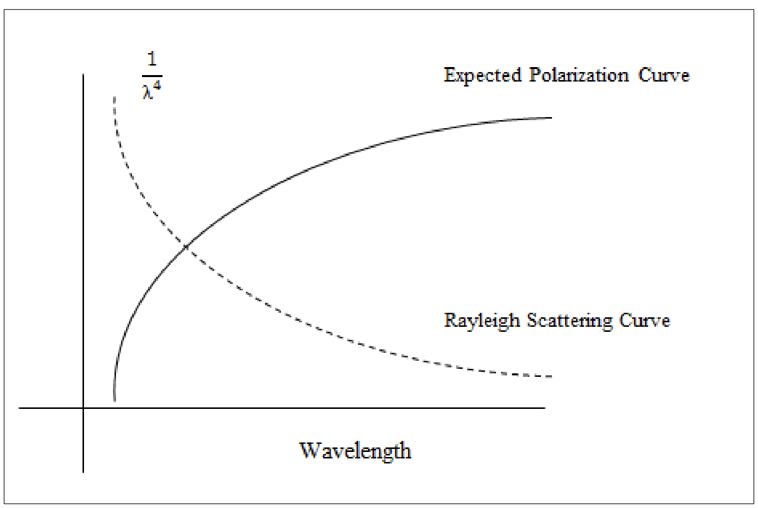

Figure 17. Conceptual relationship between Rayleigh scatting theory and polarization.

To model a Rayleigh atmosphere, the aerosol optical depth was constrained to τ_{aer} = 10^{-6} for all wavelengths, making it essentially zero. The Rayleigh model also included no surface reflectance. Identical results were produced when using AERONET data products from multiple days with the same aerosol optical depth and no surface reflectance as shown in Figure 18. The degree of linear polarization in the SWIR matches what was predicted as the polarization curve increases to an upper limit of 95% (since molecular scattering is not zero, the polarization curve does not have an upper limit of 100%).

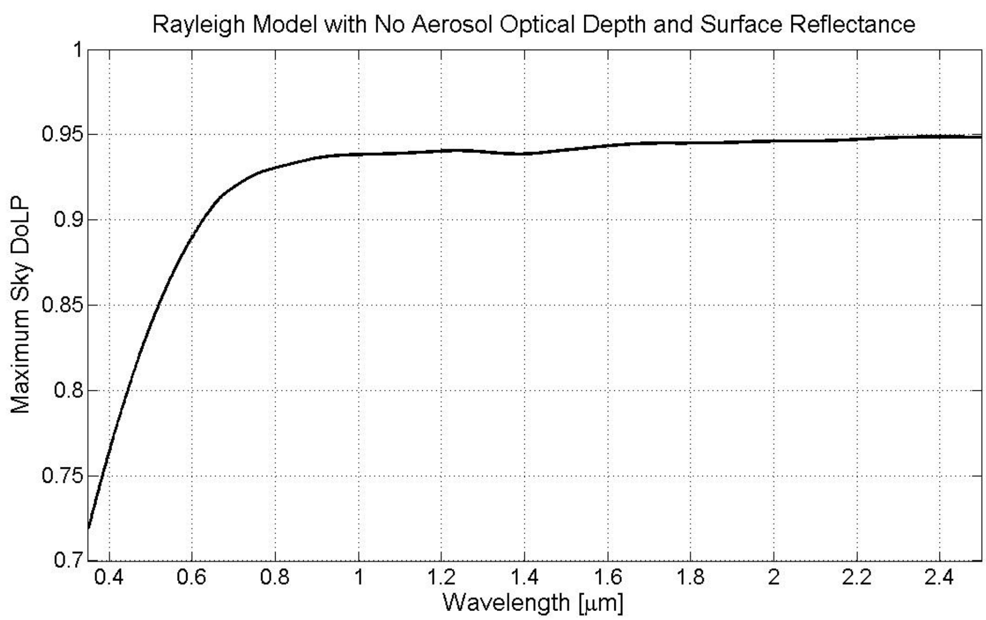

Figure 18. Rayleigh model with essentially no aerosols (τ_{aer} = 10^{-6}) and no surface reflectance.

Spectrally Constant Aerosols with No Surface Reflectance

When the aerosol optical depth becomes larger than the Rayleigh optical depth, different polarization trends arise, as seen in the four different simulations in Figure 19.

The polarization curve no longer stabilizes at 95% for long wavelengths, but instead decreases with wavelength starting at approximately 0.7 µm. The first simulation spectrally constrained the aerosol optical depth to 0.001 and used AERONET retrievals from the volume size distribution and refractive index on 3 August 2014 (smoky day). The second and third simulations used the same aerosol optical depth, but with the other aerosol parameters from 18 August 2014 (moderately hazy day) and 19 October 2014 (clean day), respectively. The final simulation used full AERONET parameters from 19 October 2014 including the actual aerosol optical depth. The only parameters that changed between the first three simulations were the aerosol volume size distribution and refractive index.

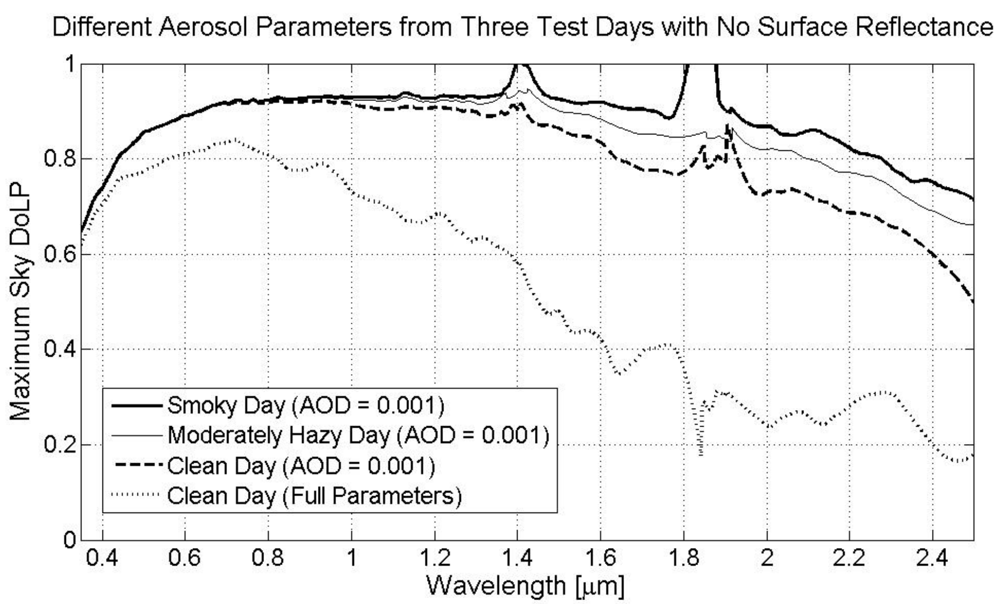

Figure 19. Maximum polarization under four different aerosol simulations with no surface. The change in polarization curve is dependent on aerosol size, the refractive index, and the phase distribution. Each case was simulated using the atmospheric parameters for the given day; however, the first three cases were run with a constant low aerosol optical depth, AOD, (τ_{aer} = 0.001) across the spectrum.

At the longer wavelengths, the DoLP varies widely for the three test days. It is important to observe that, while the polarization falls off at longer wavelengths because the aerosol optical depth is greater than the Rayleigh optical depth, it does so at different rates that are controlled by the aerosol volume size distribution. For example, the DoLP curve for 3 August remains higher than the others since most of the particles are found within the accumulation (fine) mode of the volume distribution plot. This indicates that the particles have a scattering cross section that is much smaller than the larger particles, therefore increasing the DoLP. A spectrally constant complex index of refraction ($1.5 + 15^{-3}i$) shifted the DoLP approximately 5% for 3 August, suggesting that the SWIR polarization also depends somewhat on the aerosol refractive index; however, the influence of the index also depends on the particle size distribution as the index change had no effect on 18 August or 19 October. Further analysis needs to be performed to fully quantify the correlation between clean versus smoky air and complex index of refraction. A decrease in refractive index tended to increase DoLP and vice versa; however, this was only observed for the wavelength range of 2 to 2.5 μm. This tends to be the range with the most uncertainty in refractive index because of the rotational-vibrational absorption bands of the aerosols.

Using the full parameters from 19 October demonstrates that while the air is extremely clean, as seen by the low fine and coarse modes in the volume size distribution, the aerosol optical depth is approximately 10 times greater than the constrained (~zero) aerosol optical depth, resulting in a strong decrease of DoLP at longer wavelengths (i.e., even on this very clean day, aerosol scattering is dominant in the

SWIR). This pattern is further explored in Figure 20, where each simulation used parameters from 18 August 2014, but with the aerosol optical depths spectrally constrained to 0.001, 0.1, and 1, respectively. This shows that generally an increase in aerosol optical depth decreases the DoLP.

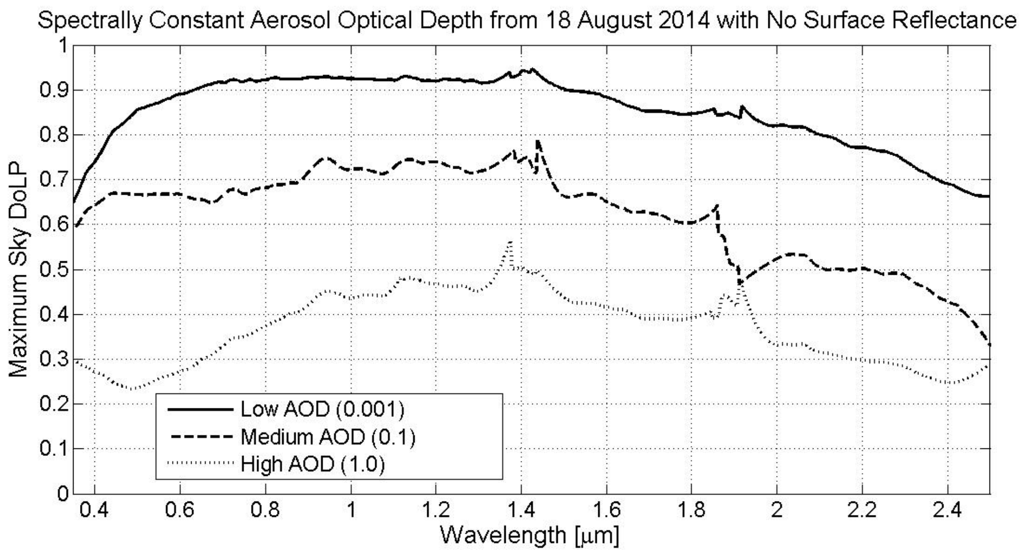

Figure 20. Degree of linear polarization for no surface and three different values of spectrally constant aerosol optical depth (AOD). Higher aerosols tend to cause lower polarization by multiple scattering. These simulations used the aerosol size distribution and index of refraction from 18 August 2014.

Aerosol Parameters from Three Test Days with No Surface Reflectance

So far we have established that for each simulated day the different relative values of aerosol and Rayleigh optical depths affect the overall modeled skylight DoLP. Figure 21 shows the relationships between the aerosol and Rayleigh optical depths for the three test days. The Rayleigh optical depths stay constant on all days, but the aerosol optical depths change dramatically. Table 3 provides the exact values for the Rayleigh and aerosol optical depths at specific wavelengths, along with a ratio between the two values.

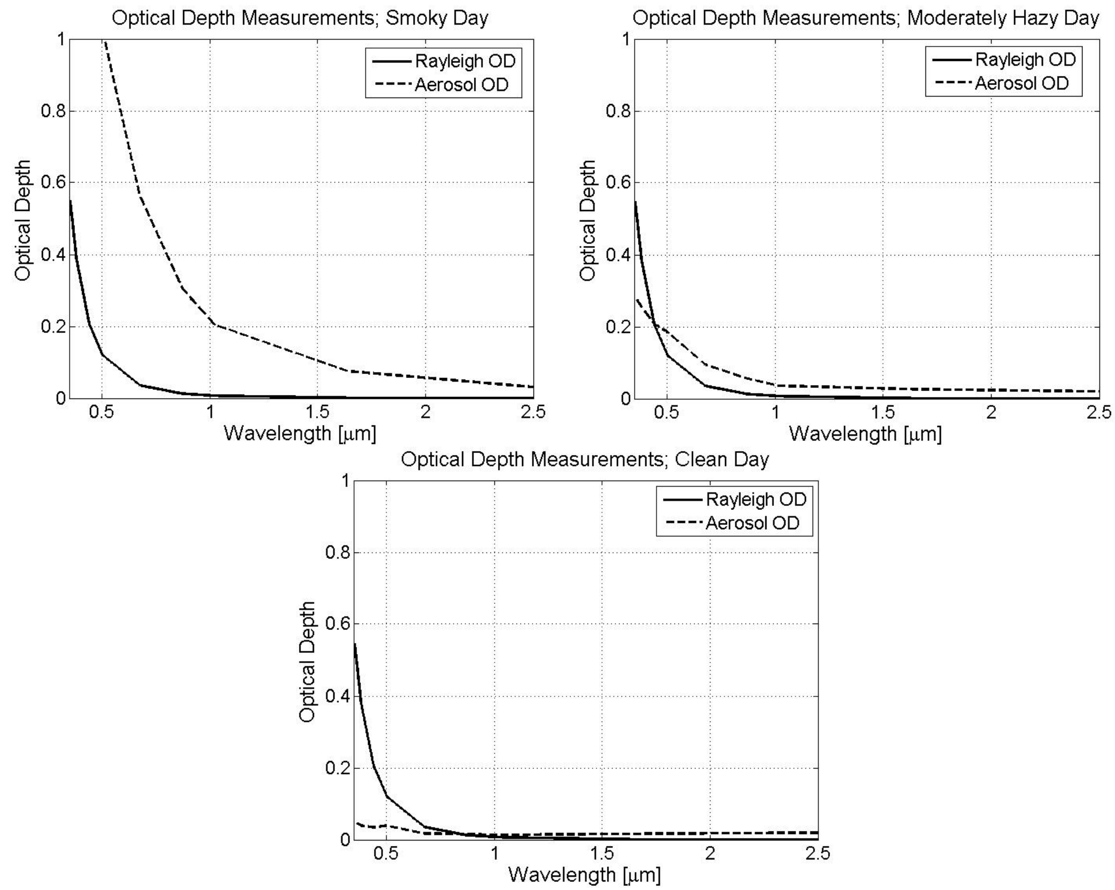

Figure 21. Comparison of aerosol optical depth and Rayleigh optical depths for 3 August 2014, smoky day (Top left), 18 August 2014, moderately hazy day (Top right), and 19 October 2014, clean day (Bottom). The aerosol optical depth and Rayleigh optical depth curves cross for 18 August and 19 October.

Day (2014)	Wavelength (μm)	Aerosol OD	Rayleigh OD	AerOD/RayOD
3 August	1.03	0.2020	0.0070	29
(Smoky Day)	1.64	0.0753	0.0010	75
	2.5	0.0310	0.0002	155
18 August	0.35	0.2840	0.5466	0.5
(Hazy Day)	1.64	0.0263	0.0010	26
	2.5	0.0199	0.0002	100
19 October	0.35	0.0473	0.5466	0.1
(Clean Day)	0.88	0.0150	0.0150	1.0
	1.64	0.0164	0.0010	16
	2.5	0.0195	0.0002	98

Table 3. Aerosol and Rayleigh optical depths with aerosol and Rayleigh optical depth ratio corresponding to Figure 21.

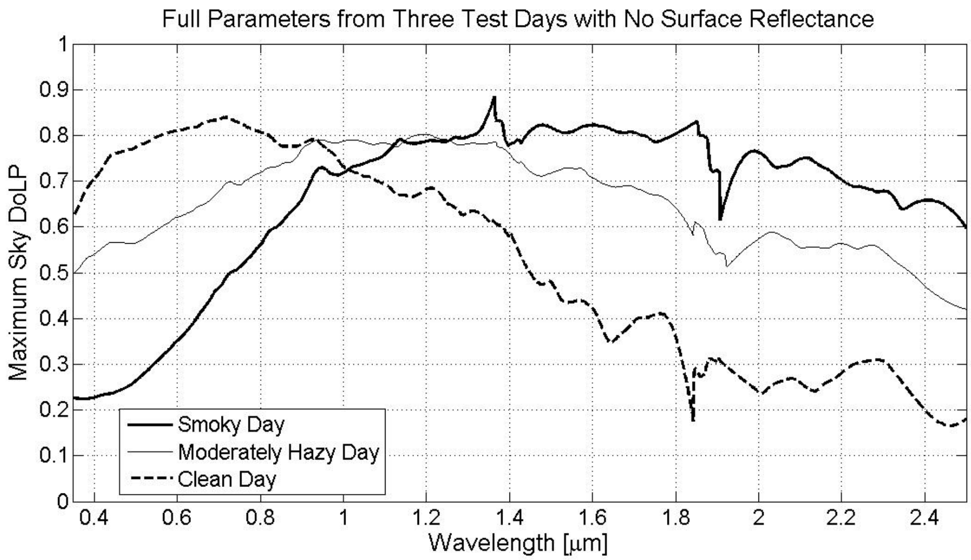

Figure 22. Degree of linear polarization for no surface reflectance and different aerosols. The polarization curve depends on the Rayleigh and aerosol optical depths. The cross-over point where the Rayleigh optical depth becomes larger than the aerosol optical depth leads to a lower polarization at longer wavelengths.

Changing aerosols have a significant effect on the polarization curve, as shown in Figure 22. Note that the “smoky” polarization curve remains well above the “clean” polarization curve that trends downward at SWIR wavelengths (even with a much larger aerosol optical depth). This appears to be a result of the very different aerosol size distributions, which suggests that it is extremely important to know the actual aerosol size distribution to accurately predict the SWIR degree of polarization. In the visible spectrum, from 0.35 to 0.5 μm, the “smoky” polarization curve is initially low since the aerosol optical depth is much greater than the Rayleigh optical depth.

Spectrally Constant Aerosols and Surface Reflectance

In the following simulations, the aerosol properties were spectrally constrained to parameters from 18 August 2014 with a low aerosol optical depth of 0.001 and the surface reflectance was kept constant across the spectrum for 0%, 10%, 50% and 90% reflectance. To validate the model, the results were compared with Coulson's measurements made at the Mauna Loa Observatory (MLO) in Hawaii in the late 1970's for an environment with low aerosols and a dark lava surface (no surface) [11]. Coulson's data covered the spectral range from 0.35 to 1.0 µm, whereas our simulations extend to 2.5 µm. It was observed that our modeled DoLP agreed well with Coulson's results.

Overall, when surface reflectance increases, the DoLP decreases, as seen in Figure 23. The decrease in polarization in the SWIR is dependent on the aerosol size distribution and the relative magnitudes of the aerosol and Rayleigh optical depths. The absorption bands in the right image (Figure 23) are interesting features in this study. As surface reflectance becomes greater, the overall DoLP decreases; however, the absorption band polarization doesn't decrease as much as the surrounding wavelengths. Surface reflection creates multiple scattering within the atmosphere that ultimately lowers the DoLP in the surrounding wavelengths, but the absorption within the band reduces this multiple scattering, leading to a higher polarization [14].

Modeling with molecular absorption adds realistic atmospheric effects to the skylight DoLP curves shown in Figure 23. When building a polarimeter, these bands need to be considered in choosing which wavelengths to measure. The absorption bands are primarily from water vapor and a general transmission spectrum with different absorption bands is shown in Figure 16. In the visible spectrum, there is a difference between the left and right images (Figure 23) where molecular ozone absorption pulls the DoLP down in the wavelength range of 0.35 to 0.7 μm.

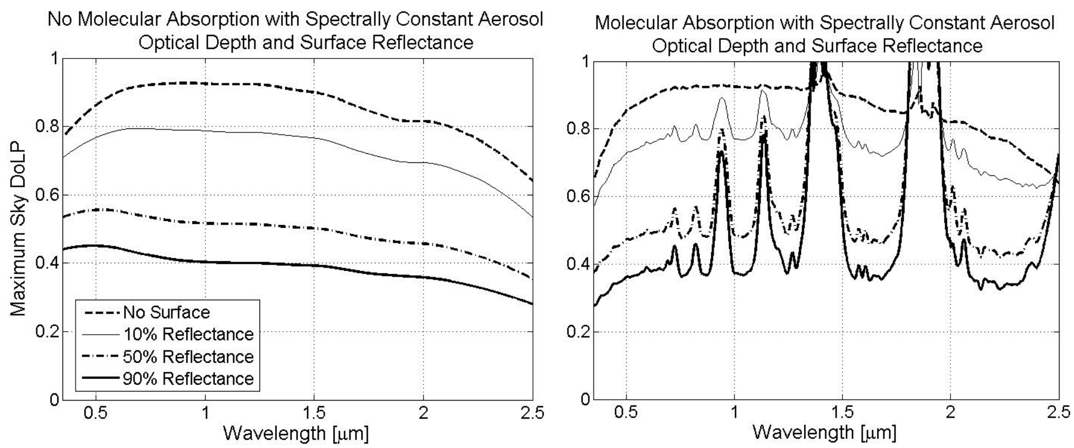

Figure 23. The maximum skylight DoLP for simulations with four changing surfaces and low aerosols (τ_{aer} = 0.001) without molecular absorption (Left) and with molecular absorption (Right). The simulations used 18 August 2014 atmospheric properties.

Spectrally Constant Aerosols with Different Measured Surface Reflectance

Differences arising in the modeled DoLP from different surface materials can be observed in Figure 24, which shows simulations using actual surface reflectance measurements of green grass, sand, a golden-yellow wheat field, and a wood surface. For each simulation, aerosol properties were constrained to parameters from 18 August 2014 and an aerosol optical depth of 0.001.

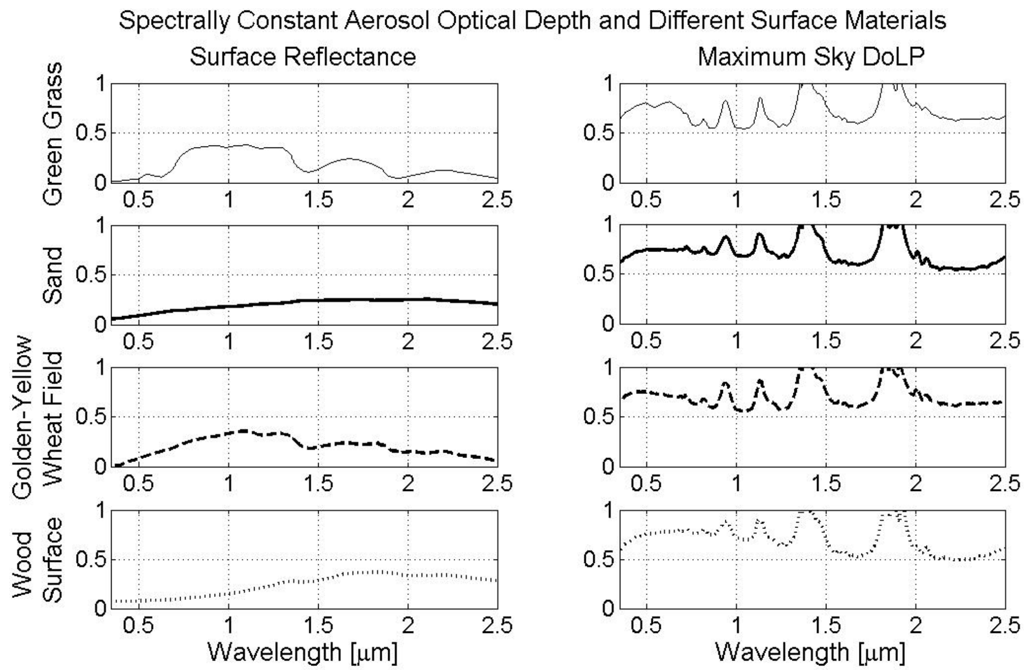

Figure 24. Maximum skylight degree of linear polarization for low aerosols (τ_{aer} = 0.001) and for different surface materials: green grass, sand, a golden-yellow wheat field, and a wood surface. Since the model was run with aerosol parameters from 18 August 2014, the general polarization curve starts at the same location and follows a similar trend, but it has changing spectral dependence arising from the underlying surface material. When surface reflectance is high, skylight polarization decreases and vice versa.

From previous studies, it is known that higher surface reflectance leads to lower sky polarization. For green vegetation, the absorption bands of chlorophyll are responsible for low reflectance values in the λ = 0.4 to 0.55 μm and λ = 0.65 to 0.69 μm regions, corresponding to a polarization maximum [11]. As seen in the wheat field reflectance spectrum, in seasonal senescence (fall), chlorophyll production decreases and leads to a lack of pigmentation. Absorption is therefore less in the chlorophyll bands, leading to higher reflectance in the green and red spectra and lower sky polarization. A spectrally constant increase in reflectance leads generally to a constant polarization change. The wood surface reflectance spectrum is interesting in that it increases in the longer wavelengths and its low visible spectrum reflectance results in the polarization remaining relatively high compared to the curves for other surface materials.

<u>Aerosol Parameters from Three Test Days with Measured Surface Reflectance</u>

Figure 25 displays the results when modeling full parameters from 3 August 2014, 18 August 2014, and 19 October 2014 using a green grass (left) and a sand (right) surface reflectance. Generally, polarization is dependent on aerosol optical depth and specific features in the DoLP curves are dependent on surface reflectance. The aerosol size distribution is the dominant controlling factor for the position of the polarization curve in the SWIR spectrum, but the surface reflectance describes the shape and trend of the curve.

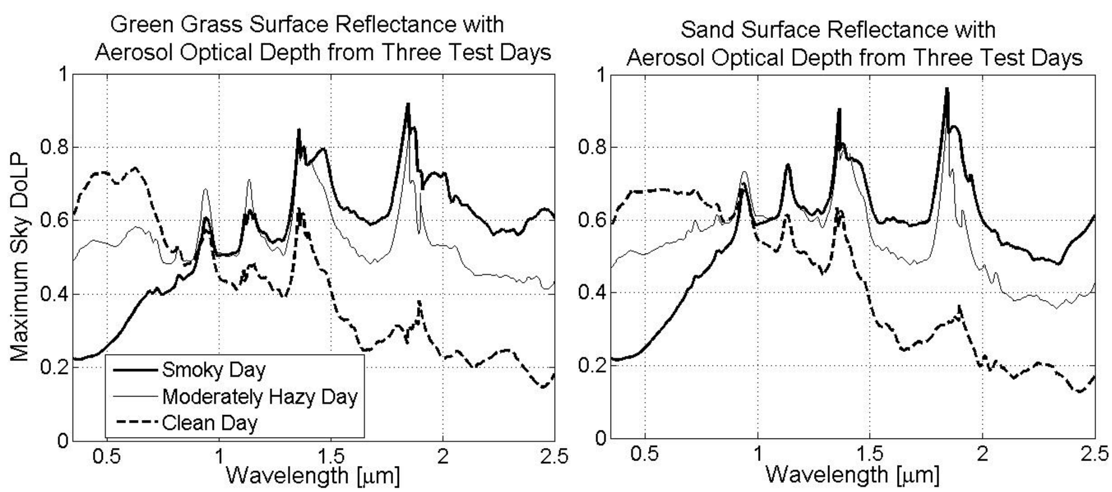

Figure 25. Realistic polarization cases for different aerosols and green grass surface reflectance (Left) and sand reflectance (Right).

4. SWIR POLARIMETER RESULTS VERSUS SOS MODEL

3 October 2014

SWIR Polarimeter Results

A SWIR polarimeter was used to image a non-resolved plane (pixels on target ≥ 4) and the surrounding skylight polarization in the SWIR, specifically in the wavelength range of 1.5 to 1.8 µm. The polarization measurement was made at 1:28 PM (MDT) in Bozeman, Montana (Cobleigh Hall, Montana State University), where the outdoor air temperature was approximately 16 ^{0}C (60^0 F). At the time the images were taken, the sun was directly above (south of the sensor and slightly west) and behind the imager, as seen in Figure 26. The solar elevation angle was 40°, with an azimuth angle of 185°. These angles are displayed in Figure 27, with the azimuth angle being measured clockwise from true north to the point on the horizon directly below the object and the elevation angle being measured vertically from the point on the horizon up to the object.

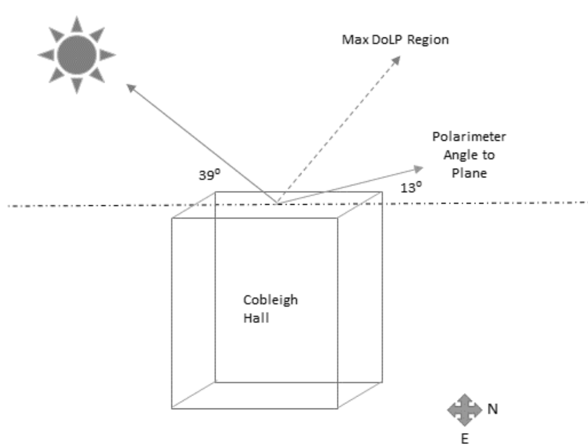

Figure 26. Diagram representing the position of the sun with respect to the image. Images were taken in Bozeman, Montana (Cobleigh Hall, Montana State University). The maximum skylight DoLP is generally located 90° from the sun.

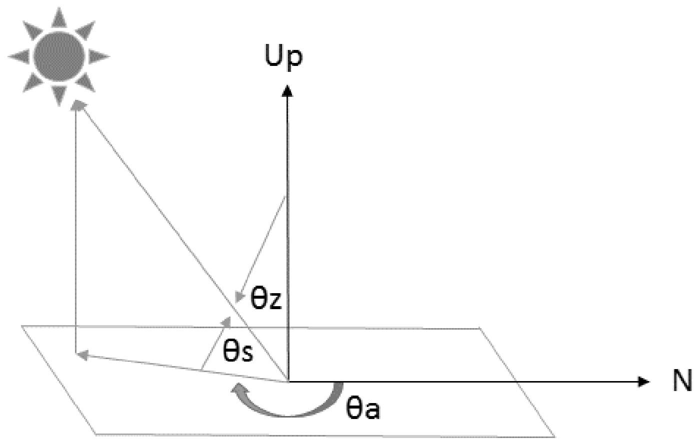

Figure 27. Coordinate representation of the azimuth angle (θ_a), sun elevation angle (θ_s), and zenith angle (θ_z).

The polarimeter had a low slant angle above the horizon and was directed slightly northwest (slant angles greater than 30^0 produced low-quality images because the liquid nitrogen no longer sufficiently cooled the focal plane array). The plane's elevation angle was determined using the visible reference images in Figure 28. Using the pixels from the brick's vertical height, the reference degree-to-pixel ratio was found to be 3.3° per 120 pixels. The airplane was 460 pixels above Cobleigh Hall (horizon reference point), therefore making the airplane's elevation angle 13^0 with respect to the horizon.

Figure 28. Both images were taken with the same un-zoomed iPhone. (Left) Polarimeter line of sight. The black line indicates the number of pixels (460) from the horizon reference point to the airplane in the sky. (Right) Reference image: used to determine the plane's elevation angle. The average brick was found to be 501 pixels by 240 pixels (0.39 m by 0.19 m). The image was taken 1.65 m away from the wall. The degree-to-pixel ratio was determined to be 3.3° per 120 pixels.

In Figure 29, the angles with respect to the horizon viewed in the polarimetric images ranged from 17.6^{0} to 11.7^{0} in the vertical axis (top-down). They were calculated by using pixel ratios from the polarimetric images with reference to the airplane's elevation angle and by knowing the polarimeter's field of view (9.1^{o} by 7.3^{o}). A more formal mapping of pixels could have been performed to ensure exact angles within uncertainty; however, an approximation was only needed in order to compare the SWIR polarimeter with the SOS model.

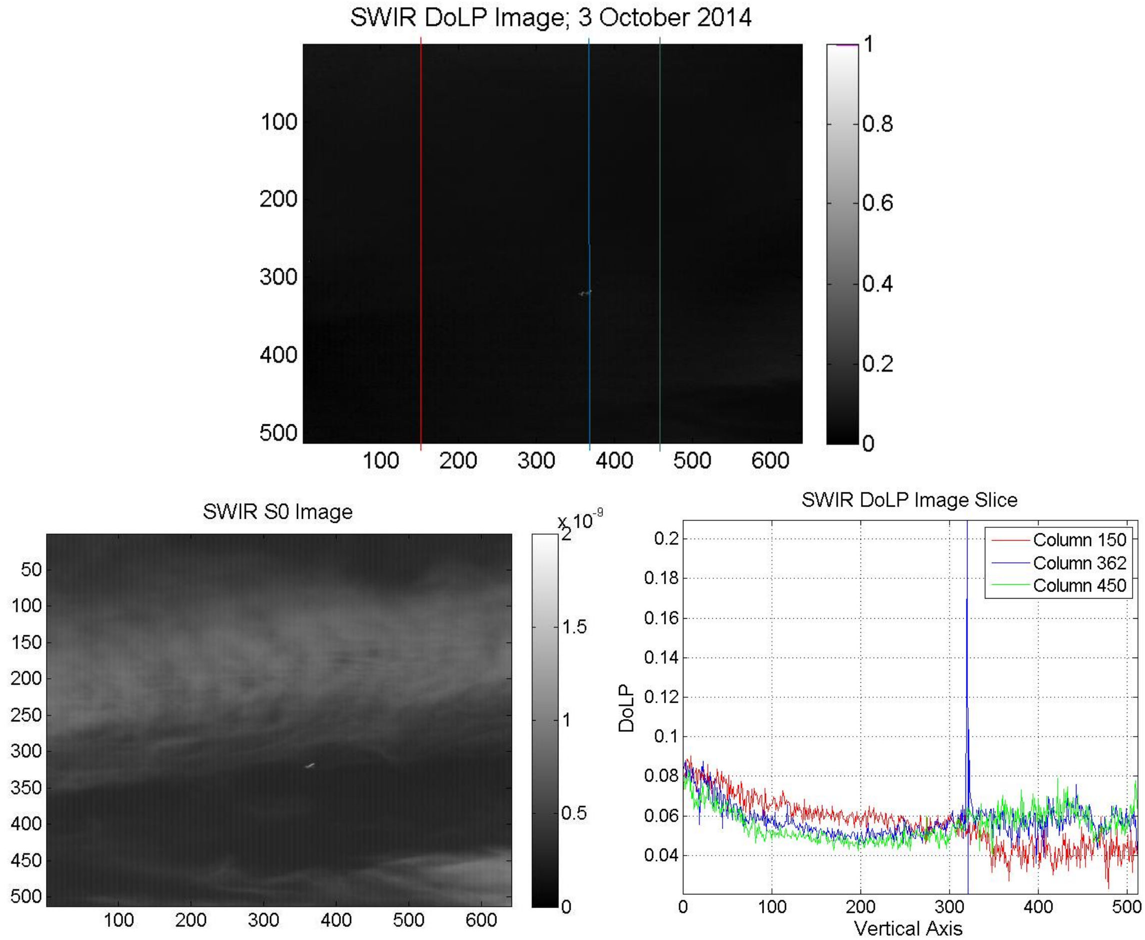

Figure 29. (Top) SWIR-MWIR polarimeter DoLP adjusted image from 3 October 2014. (Bottom left) Radiance image. (Bottom right) DoLP slice. The horizontal axis corresponds to the vertical axis in the DoLP and radiance images. The plane's DoLP was 0.69.

The vertical DoLP slices in Figure 29 show the maximum sky polarization to vary from approximately 8 to 4% (top to bottom) and to decrease within the cloud. The DoLP slice for column 150 is lower than columns 362 and 450 from the lingering cirrus cloud in its path. The airplane was found to be 69% polarized.

Model Simulation and Results

The simulation used AERONET data products from 3 October 2014 at 1:28 PM (MDT) and a green vegetation reflective surface. The model was also run with a golden-yellow wheat field reflective surface and similar results were produced. Figure 30 shows the corresponding Rayleigh and aerosol optical depths, along with the AERONET-retrieved aerosol volume size distribution and refractive index.

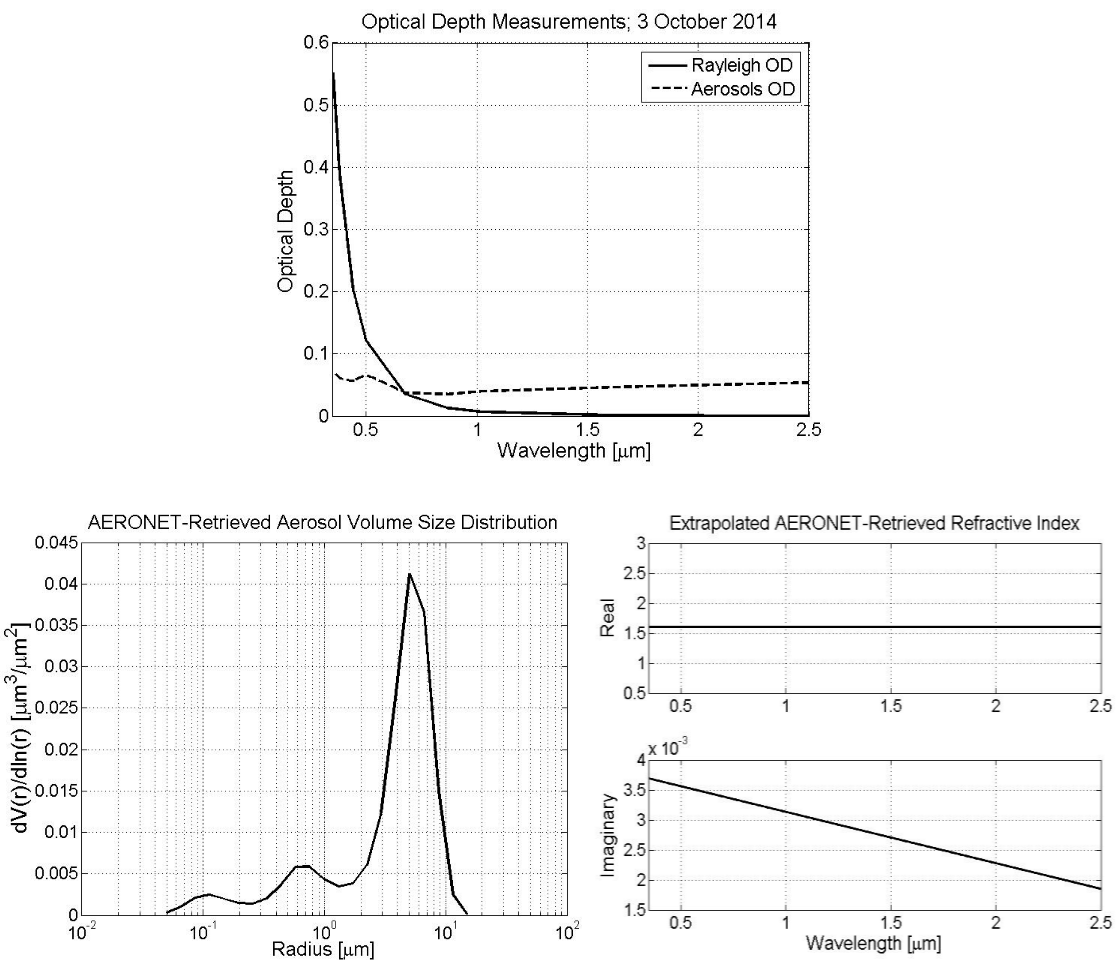

Figure 30. (Top) Rayleigh and aerosol optical depths for 3 October 2014. (Bottom Left) AERONET-retrieved aerosol volume size distribution. (Bottom right) AERONET refractive index.

The model's maximum sky polarization varied between approximately 14% and 6.7% over a wavelength range of 1.5 to 1.8 µm, as shown in Figure 31. Differences between the DoLP spectrum are noticeable in the DoLP slices through the sun and zenith for 0.5 µm and an average of slices from 1.5 to 1.8 µm in increments of 0.05 µm. The visible spectrum has a higher maximum DoLP than the SWIR spectrum and more variations within the slice occur in the SWIR spectrum. The lobes within the slices are not uncommon for longer wavelengths and are usually smoothed by multiple scattering at shorter wavelengths [29]. From the volume size distribution, most particles are in the coarse mode, indicating that the particles are large and dense. The fluctuations with angle are essentially showing that the angular scattering pattern is not smooth like it is for small (Rayleigh) particles.

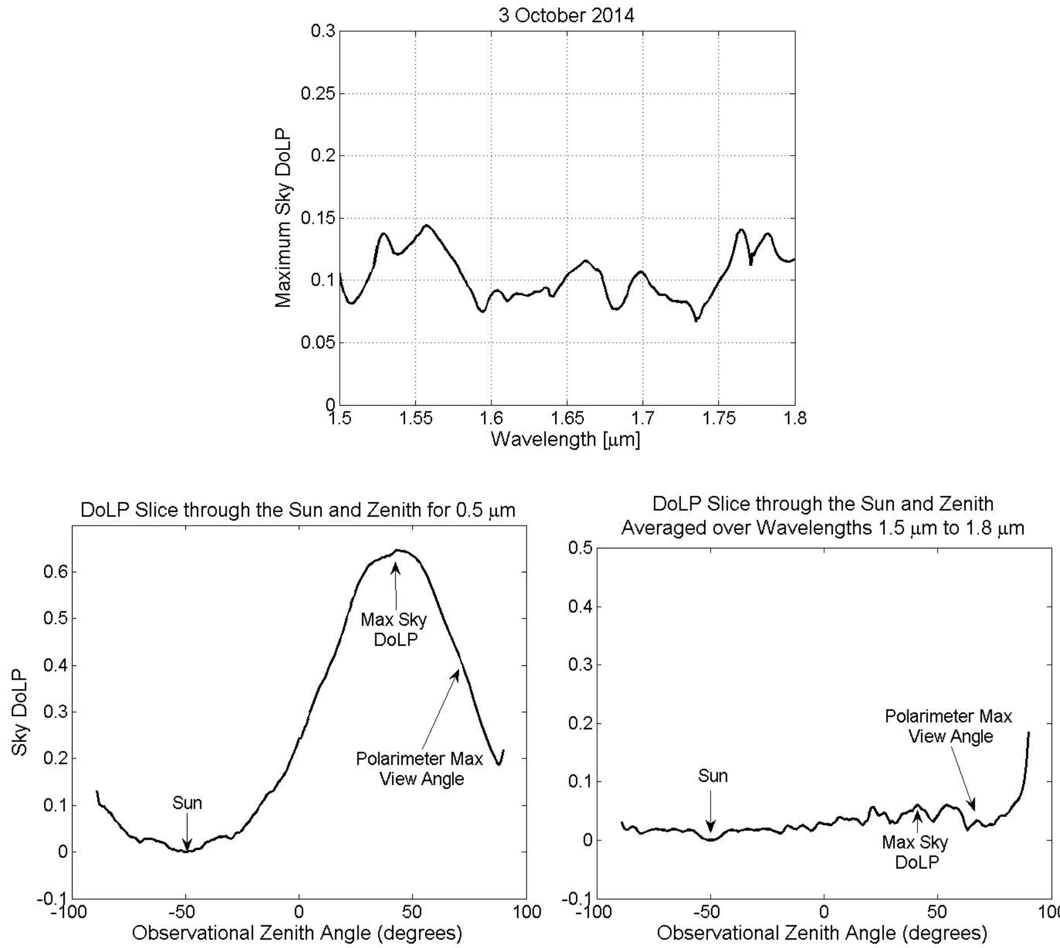

Figure 31. (Top) Modeled DoLP dependence from 1.5 to 1.8 µm for 3 October 2014 using AEROENT data products and a green vegetation reflective surface. (Bottom left) A slice of the DoLP through the sun's zenith angle and principal plane for 0.5 µm. (Bottom right) An average slice of the DoLP through the sun's zenith angle and principal plane from 1.5 to 1.8 µm in 0.05 µm increments.

The sky DoLP at an angle of 17.6^0 with respect to the horizon was found to be approximately 8% with the SWIR polarimeter (Figure 29) and 3% in the slice averaging between wavelengths of 1.5 to 1.8 µm (Figure 31). The model and the polarimeter both observed the skylight DoLP to decrease top-down.

20 April 2015

SWIR Polarimeter Results

Focusing on SWIR skylight polarization in the wavelength range of 1.5 to 1.8 μm, a measurement was made at 12:14 PM (MDT) on 20 April 2015 once again in Bozeman, Montana (Cobleigh Hall) with the SWIR polarimeter. Viewing a clear sky with clouds forming on the mountains in the distance, the polarimeter was directed towards the northwest as shown in Figure 32. The solar elevation angle was 53° with an azimuth angle of 151° and the sun’s position was behind and to the left of the imager.

Figure 32. (Left) Position of the sun with respect to the polarimeter. (Right) The polarimeter was directed towards the north-west and as seen in the left and right images, clear sky was present in Gallatin Valley with clouds forming on the mountains in the distance. The solar elevation angle was 53° with an azimuth angle of 151°. The measured images were taken at 12:14 PM (MDT) in Bozeman, Montana (Cobleigh Hall, Montana State University).

The DoLP image in Figure 33 shows polarization present in the clear portions of the sky, with clouds producing depolarizing effects. The maximum degree of polarization is predicted to occur approximately 90° from the sun at 143^0 which occurs 37^0 above the horizon. For reference in the image, the cirrus (wispy) cloud was approximately 3.5^0 above the edge of Cobleigh Hall, taken to be the horizon reference. This was determined by using an iPhone image and comparing it with a reference. The degree-to-pixel ratio was found to be 10.1^0 per 540 pixels. The angles with respect to the horizon reference viewed in the polarimetric images ranged from 6.7^0 to -0.6^0 in the vertical axis (top-down).

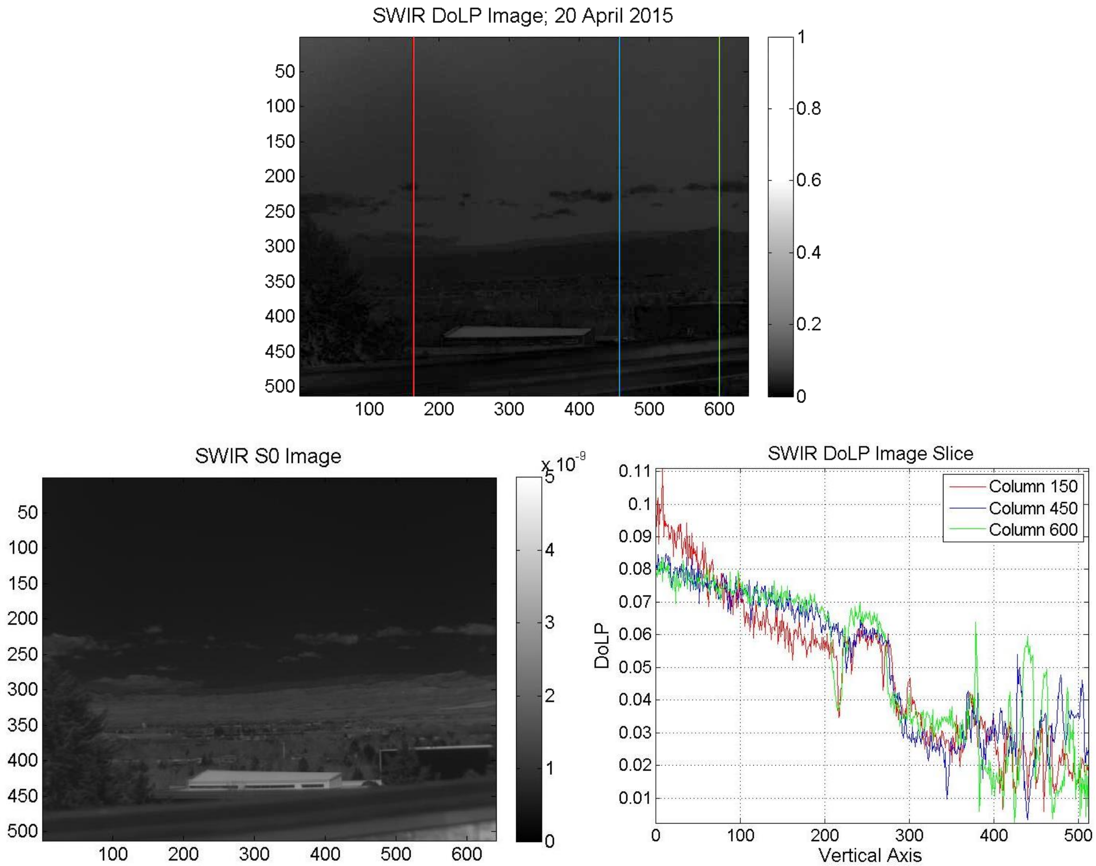

Figure 33. (Top) SWIR-MWIR polarimeter DoLP adjusted image from 20 April 2015. (Bottom left) Corresponding radiance image. (Bottom right) DoLP slice. The horizontal axis corresponds to the vertical axis in the DoLP and radiance images.

The DoLP slice in Figure 33 shows the measured sky polarization to be approximately 10% at the top of the image, with a minimum of approximately 1% at the bottom of the image. The polarization decreases at the cloud layer and then it drops significantly at the mountain position. The polarization finally rises over the green field and becomes relatively constant.

<u>Model Simulation and Results</u>

The simulation used AERONET data products from 20 April 2015 at 12:14 PM (MDT) and a green vegetation reflective surface. Figure 34 shows the corresponding Rayleigh and aerosol optical depth along with the AERONET-retrieved aerosol volume size distribution and refractive index.

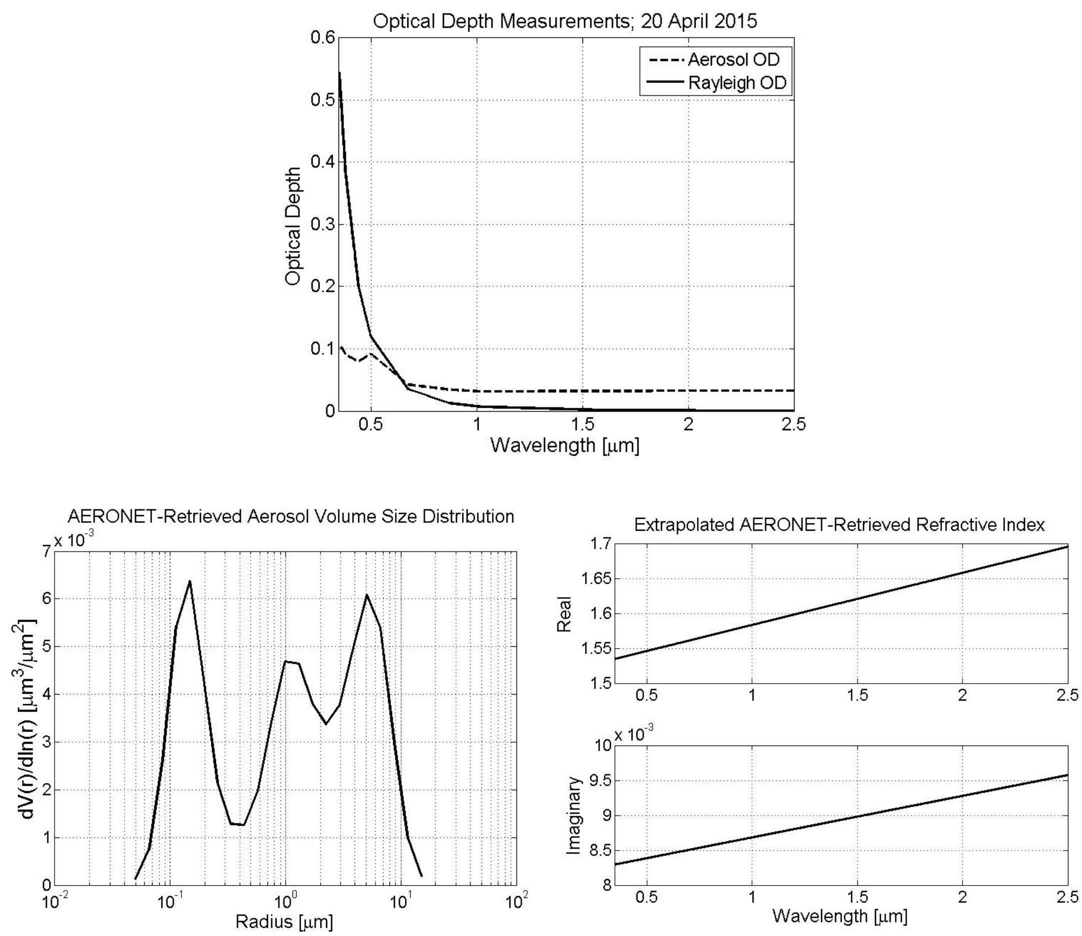

Figure 34. (Top) Rayleigh and aerosol optical depths for 20 April 2015. (Bottom Left) AERONET-retrieved aerosol volume size distribution. (Bottom right) AERONET refractive index.

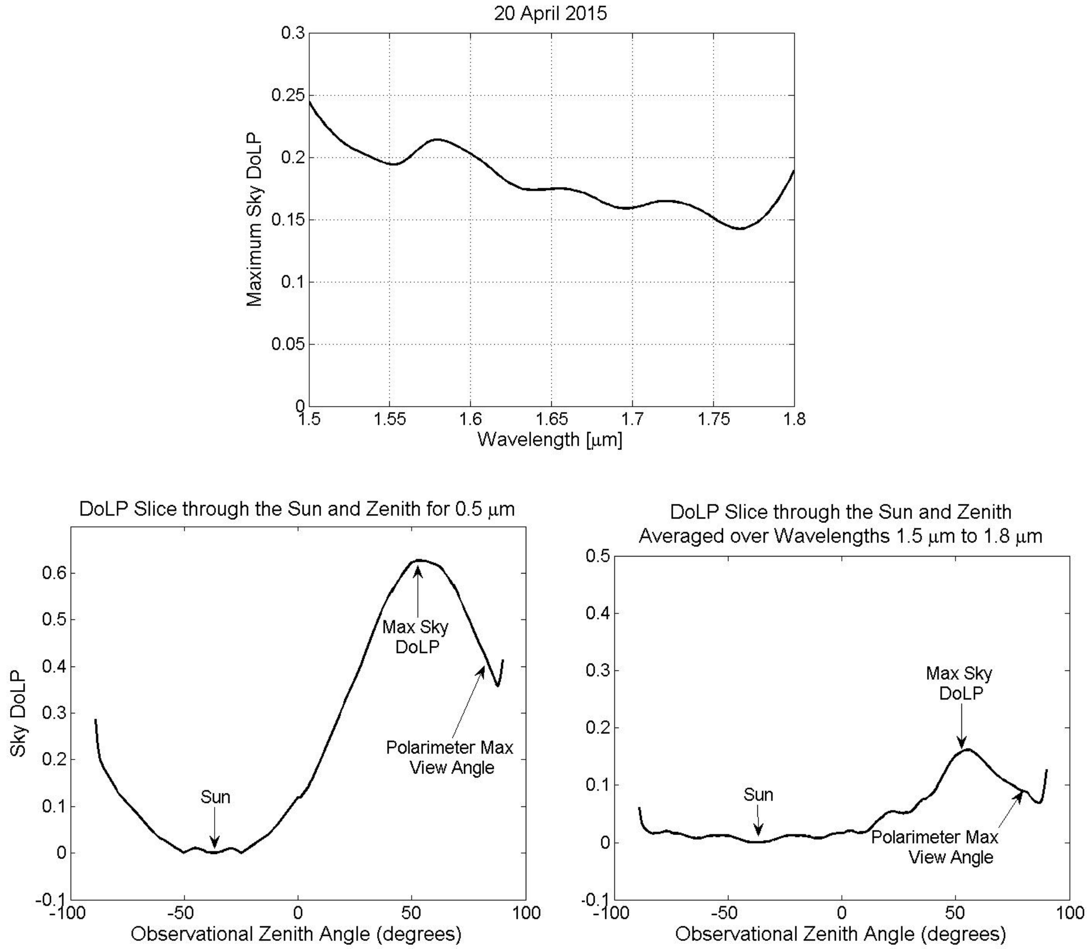

Figure 35. (Top) Modeled DoLP dependence from 1.5 to 1.8 μm for 20 April 2015 using AERONET data products and a green vegetation reflective surface. (Bottom left) A slice of the DoLP through the sun's zenith angle and the principal plane for 0.5 μm. (Bottom right) An average slice of the DoLP through the sun's zenith angle and principal plane from 1.5 to 1.8 μm in 0.05 μm increments.

The model's maximum sky polarization varied between approximately 26% and 13% for a wavelength range of 1.5 to 1.8 μm, as shown in Figure 35. At 6.7^0 above the horizon, the maximum degree of linear polarization indicated in the averaged DoLP slice is approximately 8% between 1.5 and 1.8 μm. This value agrees well with the SWIR polarimeter's measurement of maximum sky polarization between 8-10% at 6.7^0.

28 April 2015

SWIR Polarimeter Results

A final measurement of SWIR skylight polarization in the wavelength range of 1.5 to 1.8 µm was made at 10:18 AM (MDT) on 28 April 2015 in Bozeman (Cobleigh Hall). The polarimeter was directed toward the northeast and, as shown in Figure 36, the sky was clear except for clouds forming over the mountains. The solar elevation angle was 41° with an azimuth angle of 114°. Therefore, the maximum polarization occurred at 131^{0} in the solar principal plane, corresponding to an elevation angle of 49^{0} from the horizon. The sun was behind and to the right of the imager, as shown in the left image.

Figure 36. (Left) Position of the sun with respect to the polarimeter. (Right) The polarimeter was directed towards the north-east and as seen in the left and right images, clear sky was present with clouds forming on the mountains in the distance. The solar elevation angle was 41° with an azimuth angle of 114°. The measured images were taken at 10:18 AM (MDT) in Bozeman, Montana (Cobleigh Hall, Montana State University).

In Figure 37, the sky DoLP decreased top-down from 13% to approximately 3%. The polarimeter field of view ranged from 9.1^0 to 1.8^0 with respect to the horizon. In the DoLP slice image, there is an approximate drop of 3% in DoLP from the top of the image to the mountain.

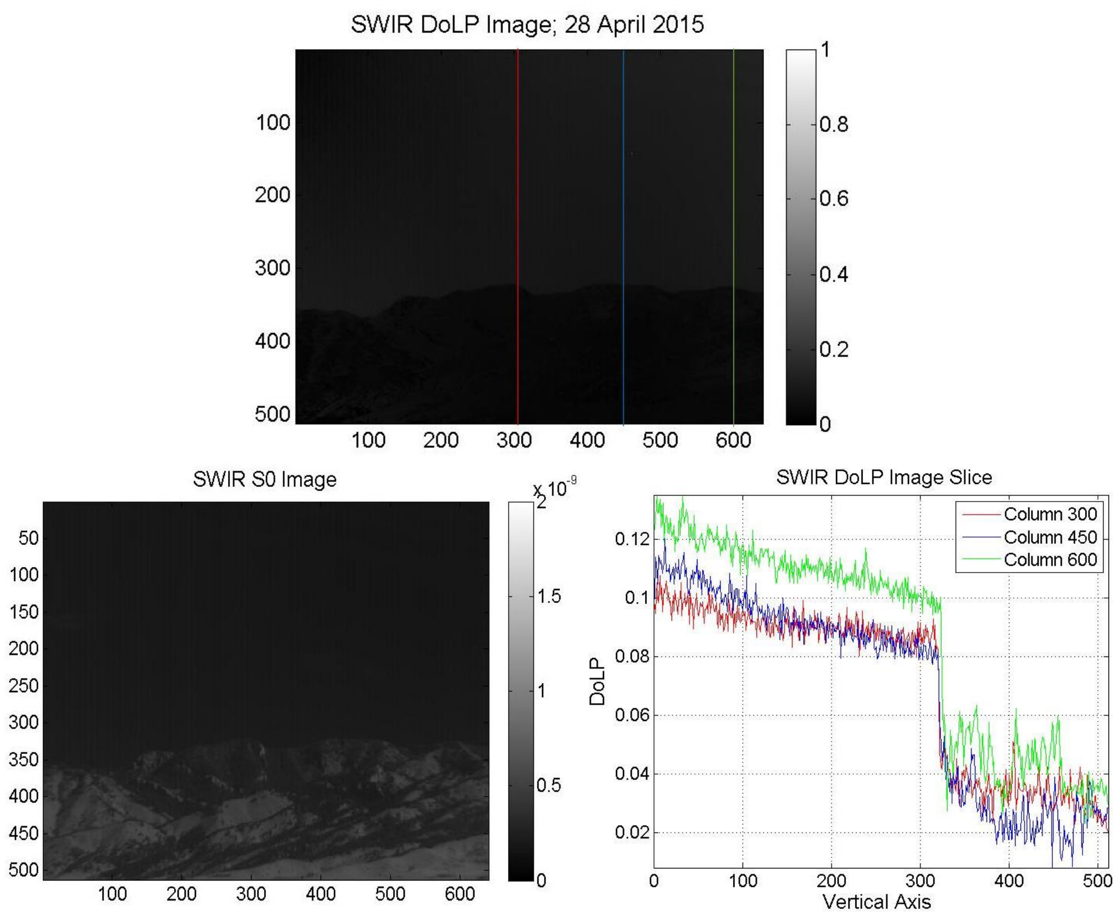

Figure 37. (Top) SWIR-MWIR polarimeter DoLP adjusted image from 28 April 2015. (Bottom left) Corresponding radiance image. (Bottom right) DoLP slice. The horizontal axis corresponds to the vertical axis in the DoLP and radiance images.

Model Simulation and Results

The simulation used AERONET data products from 28 April at 10:18 AM (MDT) and used a green vegetation reflective surface. Figure 38 shows the corresponding Rayleigh and aerosol optical depth along with the AERONET-retrieved aerosol volume size distribution and refractive index.

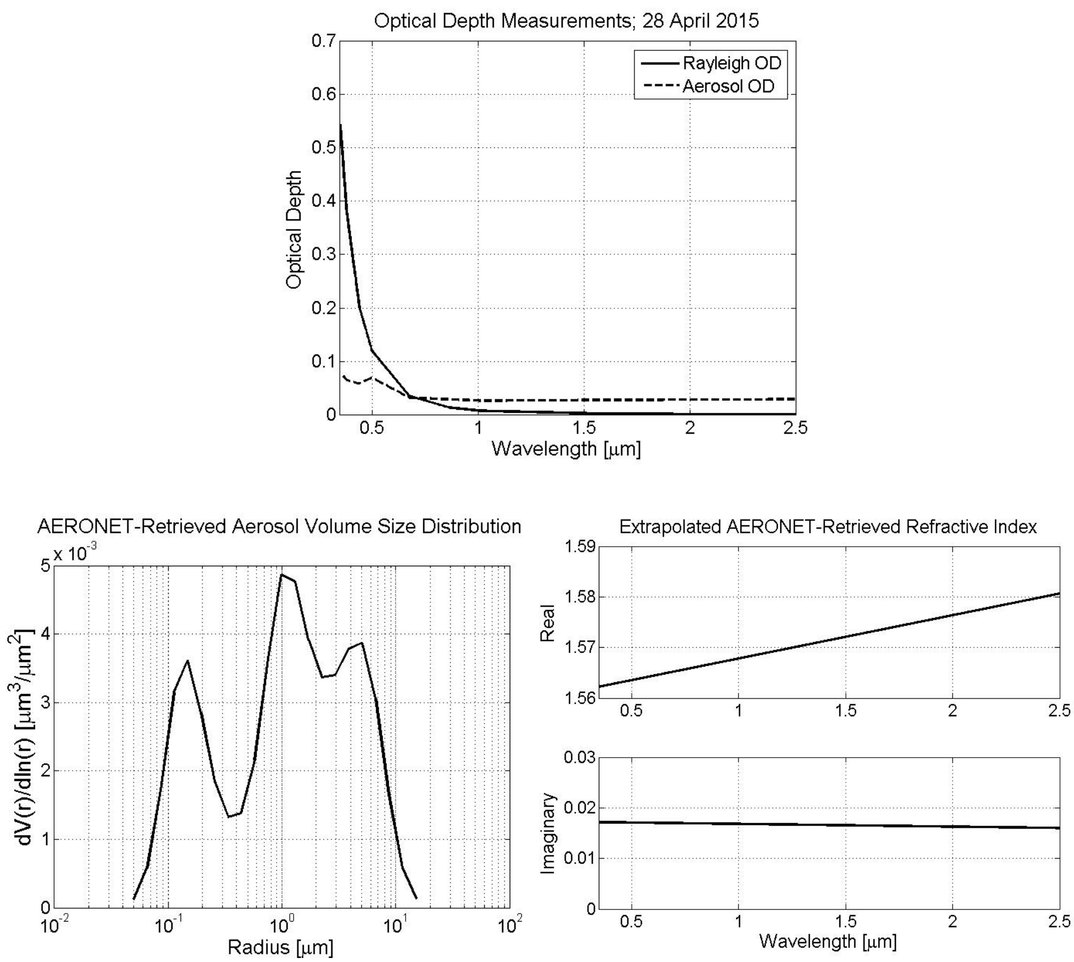

Figure 38. (Top) Rayleigh and aerosol optical depths for 28 April 2015. (Bottom Left) AERONET-retrieved aerosol volume size distribution. (Bottom right) AERONET refractive index.

The model's maximum sky polarization varied between approximately 34% and 27% for a wavelength range of 1.5 to 1.8 µm, as shown in Figure 39. At 9.1^0 with respect to the horizon, the SWIR polarimeter measured a sky polarization between 10 to 13%, while the model predicted a maximum sky DoLP of 7% which was found using the average zenith slice representing the wavelengths between 1.5 and 1.8 µm.

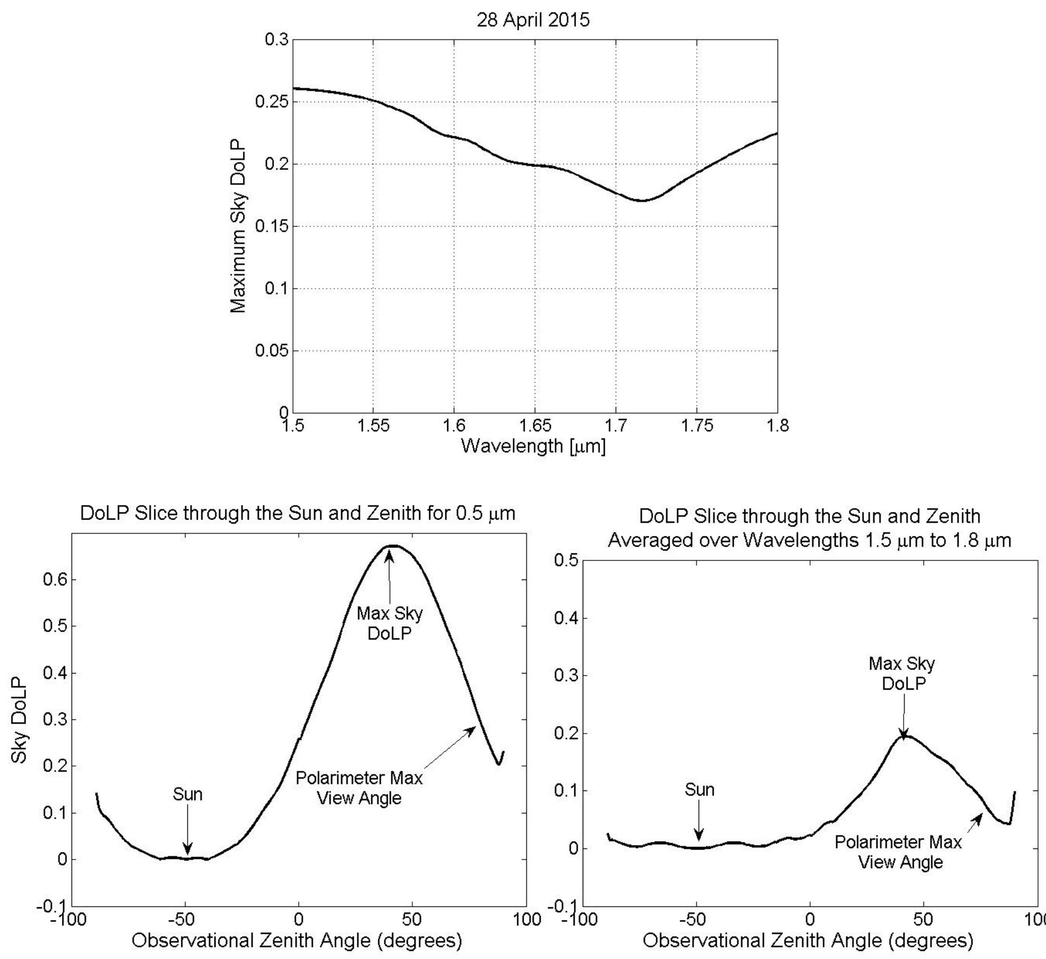

Figure 39. (Top) Modeled DoLP dependence from 1.5 to 1.8 µm for 28 April 2015 using AEROENT data products and a green vegetation reflective surface. (Bottom left) A slice of DoLP through the sun's zenith angle and principal plane for 0.5 µm. (Bottom right) An average slice of the DoLP through the sun's zenith angle and principal plane from 1.5 to 1.8 µm in 0.05 µm increments.

The model agrees relatively well with the SWIR polarimeter. Differences could arise from using Cobleigh Hall as the reference horizon point and by approximating the viewing angles of the polarimeter rather than using a pixel mapping method. Aerosol particles were also assume to be spherical within the model which could have caused errors and the SWIR polarimeter measured between the range of 1.5 to 1.8 μm which is between two large absorption bands possibly causing the DoLP to be different as seen with the previous models.

5. CONCLUSION

This work contributed significantly to characterizing skylight polarization in the SWIR spectrum, a region not commonly studied. A successive-orders-of-scattering radiative transfer model was modified to include AERONET data products and surface reflectance measurements taken with a hand-held spectrometer. Extrapolation of aerosol parameters was performed in order to model skylight polarization in the VIS-SWIR spectrum (350 to 2500 nm). The model estimated the degree of linear polarization in the clear sky and modeled results were compared against SWIR measurements taken with the Corvus SWIR-MWIR polarimeter. Generally the two methods showed clear-sky DoLP decreasing in the SWIR spectrum and agreed relatively with one another.

The modeled visible to short-wave-infrared maximum polarization of skylight is dependent on the ratio of the aerosol and Rayleigh optical depths, is highly dependent on the aerosol volume size distribution, and has unique spectral features associated to the reflectance spectrum. As aerosol optical depths increased, the degree of linear polarization spectrum generally decreased with wavelength at a rate dependent on the aerosol size distribution and the DoLP no longer followed the expected Rayleigh scattering model.

The SOS model can be improved by modifying the code to include both spherical and non-spherical particles. For simplicity in the current model, only spherical particles were assumed with Mie scattering; however, not all particles are spherical in nature and a more accurate model of the real atmospheric environment could benefit from this being changed. Performing a more concentrated analysis of the aerosol complex index of refraction in the SWIR spectrum could be done. For instance, does the DoLP consistently increase a certain amount when a 5% bias is added to the complex refractive index? It was observed that a change in refractive index altered the skylight DoLP in the SWIR spectrum between 2-2.5 µm for larger aerosol optical depths, but not for smaller optical depths. A relationship between aerosol refractive index, optical depth, and DoLP could be quantified with more analysis. Further validation experiments using the Corvus SWIR-MWIR polarimeter could help justify that the model and the instrument are reporting the same results. If a pixel mapping algorithm was used in the analysis of the SWIR Polarimeter's images, improved results between the model and polarimeter may also be seen.

This study demonstrated that accurate predictions of SWIR skylight polarization depend particularly strongly on knowing the aerosol particle size distribution and future work could be applied towards detecting cloud phase and using skylight polarization signatures for navigational systems. The SOS model in this study used AERONET aerosol parameters to create polarized models of the sky; however, the improved understanding produced by this study positions us to move toward retrieving aerosol parameters from SWIR polarization measurements. Polarization generally adds an additional element when imaging a scene and can be used in cloud phase detection, as well as in determining general relationships between clouds and aerosols. This benefits global climate studies, as aerosols have a significant impact on the Earth's climate. Data from the polarized measurements can be used to determine the thermodynamic phase of clouds [30] and can be used to inversely find the optical depth [31], effective radius, and refractive index [32] [33] of aerosols.

The SOS model and the SWIR polarimeter may also be useful in combination with Montana State University's Infrared Cloud Imager [34] to determine cloud optical depth and type. Polarization can be used to determine the thermodynamic phase of overlying clouds [2][30], specifically if they have liquid droplets or ice particles. Liquid and ice particles are different from one another in the sign of the S_1 Stokes parameter. Liquid phase cloud droplets have positive values of S_1 (linear polarization is perpendicular to the scattering plane) while the ice particles have negative value of S_1 (linear polarization is parallel to the scattering plane) [30].

The SOS code could be used to model skylight polarization patterns for navigational systems [35] in autonomous (i.e. unmanned aerial) vehicles that are becoming more frequently seen in the military and in the public. Polarization sensitive animals such as fish and dung-beetles use skylight polarization for navigational cues. A vehicle's location can be determined by using a polarized light sensor that measures the angle of polarization of skylight and by comparing this measurement to a single-scattering Rayleigh model. By knowing the sun's position, the heading of the vehicle can be found. This professional project was able to model and measure SWIR polarization in the sky which can be applied towards applications such as cloud phase detection, retrieval of aerosol properties, and navigation based on polarization signatures in the sky.

REFERENCES CITED

1. J. S. Tyo, D. L. Goldstein, D. B. Chenault, and J. A. Shaw, "Review of passive imaging polarimetry for remote sensing applications," Appl. Opt. **45**, 5453-5469 (2006).

2. N. J. Pust and J. A. Shaw, "Digital all-sky polarization imaging of partly cloudy skies," Appl. Opt. **47**, H190-H198 (2008).

3. J. A. Shaw, "Degree of linear polarization in spectral radiances from water-viewing infrared radiometer," Appl. Opt. **38**(15), 3157-3165 (1999).

4. N. J. Pust, A. R. Dahlberg, M. J. Thomas, and J. A. Shaw, "Comparison of full-sky polarization and radiance observations to radiative transfer simulations which employ AERONET products," Opt. Express **19**, 18602-18613 (2011).

5. J. Tyndall, "On the blue color of the sky, the polarization of skylight, and polarization of light by cloudy matter generally," Proc. R. Soc. Lond. **17**, 223-233 (1868).

6. J. W. Strutt, "On the light from the sky, its polarization and colour," Phil. Mag. **41**, 107-120 (1871).

7. L. Rayleigh, "On the transmission of light through an atmosphere containing small particles in suspension, and on the origin of the blue sky," Phil. Mag. **47**, 375-384 (1899).

8. J. Lenoble, "Scattering and Polarization of the Solar Radiation in the Earth's Atmosphere: Historical Review and Present Applications," in *Proc. of AIP*, 7-10 (2009).

9. G. Mie, "Contributions on the optics of turbid media, particularly colloidal metal solutions," Annalen der Physik. **25**, 377-445 (1908).

10. G. Mie, "Contributions to the optics of turbid media, particularly of colloidal metal solutions," Royal Aircraft Establishment, Library Translation, (1873,1976). 〈http://diogenes.iwt.uni-bremen.de/vt/laser/papers/RAE-LT1873-1976-Mie-1908-translation.pdf〉

11. K. L. Coulson, *Polarization and intensity of light in the atmosphere* (1988).

12. A. Kreuter, C. Emde, and M. Blumthaler, "Measuring the influence of aerosols and albedo on sky polarization," Atmospheric Research **98**, 363-367 (2010).

13. M. Hess, P. Koepke, and I. Schult, "Optical properties of aerosols and clouds; the software package OPAC," Am. Meteorol. Soc.**79**, 831-844 (1998).

14. E. Boesche, P. Stammes, R. Preusker, R. Bennartz, W. Knap, and J. Fischer, "Polarization of skylight in the O2A band: effects of aerosol properties," Appl. Opt. **47**, 3467-3480 (2008).

15. A. R. Dahlberg, N. J. Pust, and J. A. Shaw, "Effects of surface reflectance on skylight polarization measurements at the Mauna Loa Observatory," Opt. Express **19**, 16008-16021 (2011).

16. J. Lenoble, M. Herman, J.L. Deuzé, B. Lafrance, R. Santer, D. Tanré, "A successive order of scattering code for solving the vector equation of transfer in the earth's atmosphere with aerosols," Journal of Quantitative Spectroscopy and Radiative Transfer **107,** 479-507 (2007).

17. B. N. Holben, T. F. Eck, I. Slutsker, D. Tanre, J. P. Buis, A.Setzer, E. Vermote, J. A. Reagan, Y. J. Kaufman, T. Nakajima, F. Lavenu, I. Jankowiak, and A. Smirnov, "AERONET - A federated instrument network and data archive for aerosol characterization," Remote Sens. Environ. **66**, 1-16 (1998).

18. O. Dubovik and M. D. King, “A flexible inversion algorithm for retrieval of aerosol optical properties from Sun and sky radiance measurements,” J. Geophys. Res. **105**(D16), 20673-20696 (2000).

19. N.J. Pust and J.A. Shaw, "Wavelength dependence of the degree of polarization in cloud-free skies: simulations of real environments," Opt. Express **20**, 15559-15568 (2012).

20. Bozeman AERONET Site, http://www.aeronet.gsfc.nasa.gov/.

21. NOAA solar calculator, http://www.esrl.noaa.gov/gmd/grad/solcalc/.

22. ASD FieldSpec Pro Manual, http://support.asdi.com/Document/FileGet.aspx?f=600000.PDF.

23. J. R. Jensen, *Remote sensing of the environment: An earth resource perspective* (2006).

24. A. ÅNGSTRÖM, "The parameters of atmospheric turbidity," Tellus **16**, 64-75 (1964).

25. O. Dubovik, et al., "Application of spheroid models to account for aerosol particle nonsphericity in remote sensing of desert dust," J. Geophys. Res. **111,** (2006).

26. J. H. Seinfeld and S. N. Pandis, *Atmospheric chemistry and physics: From air pollution to climate change* (2006).

27. E. P. Shettle and R. W. Fenn, "Models for the aerosols for the lower atmosphere and the effects of humidity variations on their optical properties," Environmental Research Papers, AFGL-TR-79-0214, No. 676 (1979).

28. A. Berk, G. P. Anderson, P.K. Acharya, L.S. Bernstein, L. Muratov, J. Lee, M. Fox, S. M. Adler-Godlen, J. H. Chetwynd, M. L. Hoke, R.B. Lockwood, J. A. Gardner, T. W. Cooley, C. C. Borel, P.E. Lewis, and E.P. Shettle, "MODTRAN5: 2006 update," in *Proc. Of the SPIE* **6233**, 508-515 (2006).

29. Personal Correspondence with Dr. Nathan J. Pust (21 May 2015).

30. K. Knobelspiesse, B. van Diedenhoven, A. Marshak, S. Dunagan, B. Holben, and I. Slutsker, "Cloud thermodynamic phase detection with polarimetrically sensitive passive sky radiometers," Atmos. Meas. Tech. **8**, 1537-1554 (2015).

31. J.L Deuzé, et al., "Remote sensing of aerosols over land surfaces from POLDER-ADEOS-1 polarized measurements," J. Geophys. Res. **106**(D5), 4913–4926 (2001).

32. M. I. Mishchenko and L. D. Travis, "Satellite retrieval of aerosol properties over the ocean using polarization as well as intensity of reflected sunlight," J. Geophys. Res. **102**(D14), 16989–17013 (1997).

33. Z. Li, P. Goloub, C. Devaux, X. Gu, J. Deuzé, Y. Qiao, F. Zhao, "Retrieval of aerosol optical and physical properties from ground-based spectral, multi-angular, and polarized sun-photometer measurements," Remote Sensing of Environment **101**, 519-533, (2006).

34. J. A. Shaw and P. W. Nugent, "Physics principles in radiometric infrared imaging of clouds in the atmosphere," Eur. J. Phys. **34**, S111 (2013).

35. T. Ma, X. Hu, L. Zhang, J. Lian, X. He, Y. Wang, and Z. Zian, "An Evaluation of Skylight Polarization Patterns for Navigation," Sensors **15**(3), 5895-5913, (2015).